

Accounts

Quantum Control of Molecular Reaction Dynamics by Laser Pulses: Development of Theory and Its Application

Yukiyoshi Ohtsuki, Michihiko Sugawara,† Hirohiko Kono, and Yuichi Fujimura*

Department of Chemistry, Graduate School of Science, Tohoku University, Sendai, 980-8578

†Department of Chemistry, Faculty of Science and Technology, Keio University, Hiyoshi, Yokohama, 223-8522

(Received February 22, 2001)

In this paper, we review our recent progress in theoretical studies of quantum control of chemical reactions. Coherent interaction between the reaction system and applied laser fields is utilized to maximize the yield of a desired product (a target state). We have developed several kinds of effective theoretical methods for designing optimized ultrashort pulses for a desired reaction. One kind of control method is based on the control theory of a linearly time-invariant (LTI) system, by which the total population of the nontarget states and the total energies of the laser fields are minimized. This procedure is carried out at each successive short stage (local optimization theory), in which the time-dependent Schrödinger equation can be approximated to the equation of motion of the LTI system. Another control method is based on a tracking problem. A given trace in the tracking problem is introduced in an objective function of the quantum control. We have also developed a method using classical mechanics that provides a guiding principle for the control of a multidimensional molecular system. These methods based on local optimization theory can generate a wide variety of pulses ranging from weak field cases to strong field cases. In our treatment, $\pi-$ and chirped pulses are obtained a priori as examples of optimized pulses. These methods have been applied to control of nuclear motions on adiabatic or diabatic potential surfaces. In addition to quantum control of typical unimolecular reactions such as isomerization, predissociation of NaI and enantiomer selective preparation, we present applications to orientation of molecules and population transfer to dark states (i.e., control of intramolecular vibrational energy redistribution). Control of orientation of molecules is a prerequisite for enantiomer selective preparation. Electronic dynamics of molecules in intense laser fields such as intramolecular electron transfer on an attosecond time scale is next discussed in order to extend our methods to novel control scenarios of chemical reactions by ultrafast manipulation of electronic motions. We have developed an efficient grid point method for accurately solving the time-dependent Schrödinger equation for the electronic degrees of freedom of a molecule. This fundamental numerical tool which extends the molecular orbital description enables us to clarify the mechanisms of intense-field-electronic dynamics such as tunnel ionization and Coulomb explosions of molecules. We present applications of this method to H_2^+ and H_2 in high-intensity and electronically nonresonant low-frequency fields ($I > 10^{13}$ W cm^{-2} and $\lambda > 700$ nm). For H_2, it has been revealed for the first time that the two localized ionic states, H^-H^+ and H^+H^-, are alternately created according to the laser cycle. Such an intramolecular electronic motion induces nuclear motions (e.g., bond stretching). Possible new control schemes of electronic and nuclear dynamics utilizing electron-electron and electron-nucleus correlations are finally proposed.

The recent developments in laser technology such as pulse shaping have opened up a new research field of chemical reaction dynamics, called quantum control or coherent control of chemical reaction dynamics.[1–6] In quantum control, the coherent nature of lasers is utilized to obtain the maximum yield of a desired product of the reaction. Molecular phases or wave functions of the reaction system are controlled through coherent interaction between the reaction system and laser light. There are two fundamental approaches to quantum control of chemical reaction dynamics. One is a time-independent approach that is called coherent phase control.[7,8] Here the control utilizes interferences between two stationary laser beams originating from the same light source. The other approach is based on time-dependent theory. The time evolution of localized nuclear wave functions (wave packets) is manipulated to yield a desired product by tailored femtosecond pulses.[9–19] This is generally called quantum control. In this paper, we focus on the latter approach.[20,21]

A simple control scenario of the latter approach is shown in Fig. 1. This is called a pump-dump control scenario.[9] The idea of this control scenario originates from femtosecond chemistry. In femtosecond chemistry, we use ultrashort pulses of which the temporal widths are shorter than the vibrational periods of the chemical bonds of interest.[22,23] A femtosecond

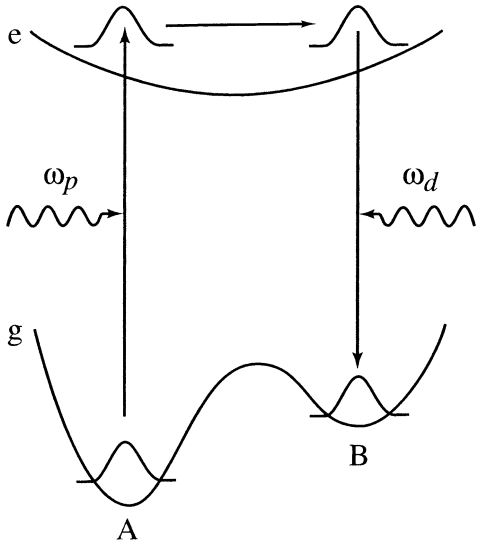

Fig. 1. Pump–dump control scenario. ω_p is the central frequency of the pump pulse, and ω_d is the central frequency of the dump pulse.

pump pulse creates a localized wave packet in an electronically excited state e from the ground state A. Then this localized wave packet is dumped into the ground state to produce the final product by applying a femtosecond control pulse when the packet moves to just above the target position B. This is the basic idea of nuclear wave packet control. In real control, in order to manipulate the wave packet on an e excited state, various scenarios have been designed to produce the maximum yield of chemical reactions.

On the other hand, as is well known, ordinary chemical reactions are controlled by changing equilibrium conditions, for example, by increasing or decreasing pressure (temperature) or using a catalytic reagent appropriate to producing a desired product. Thus, the principle of quantum control of chemical reactions founded on the coherent nature of material and light is contrasted to that of ordinary reactions. The aim of quantum control is to construct a foundation for the development of a quantum chemical engineering, which is expected to become a new chemical industry in this century. Quantum engineering utilizing precise manipulation of laser pulses in time and space domains will make an important contribution to research fields such as biochemical research as well as to nanoscale material science and technology.

In this paper, we describe the recent progress made in quantum control of chemical reaction dynamics in our laboratory. Our development of effective methods for quantum control of molecular reaction dynamics is mainly based on local control theory, in which the imposed conditions for obtaining a desired product are satisfied at each successive short stage.[18,19,24,25] Here, "effective" means that the method can design a wide variety of laser pulses ranging from weak field cases to strong field cases. In addition to control methods using quantum mechanics, a classical version has been recently developed. The classical version, which is adaptable to systems of many degrees of freedom, plays an important role in making scenarios of the control of a multidimensional molecular system.[26] We also pay attention to the mechanisms of quantum control of chemical reactions, to how such reactions are controlled by shaped pulses, and to what are the important factors to control reactions.

In the next section, the optimal control theory that has been developed is briefly described. In section 2, we present applications of our control theory to several kinds of molecular reactions, such as photodissociation of NaI,[27,28] enantiomer selective preparation,[29] and ring puckering isomerization.[18] We also present applications of our control methods to alignment and orientation control of molecules[30] and control of dark states.[21] Control of alignment and orientation of molecules is prerequisite for stereochemistry and also for enantiomer selective preparation. The control of dark states, which are not optically coupled to the ground state, enables control of energy transfer phenomena such as intramolecular vibrational energy redistribution and intersystem crossings. Our control theory is applicable to molecular reactions in strong as well as weak laser. There exist other control approaches in the case of strong laser fields, such as adiabatic rapid passage[31,32] and dressed state approaches.[33,34]

In the above treatments, empirical or calculated potential surfaces of the electronic states that are expected to participate in the process of interest are introduced beforehand. On the other hand, in intense laser fields beyond $I > 10^{13}$ W cm^{-2}, the electronic wave function is so strongly deformed within a half optical cycle that a large part of the electron density is transferred among nuclei on an attosecond scale. Such an intramolecular electronic motion induces nuclear motions (e.g., bond stretching and bending); resultant laser-induced structure deformations in turn change the electronic response to the field, e.g., ionization rates. To evaluate the electronic and nuclear dynamics in the nonperturbative regime, it is necessary to solve the time-dependent Schrödinger equation for the electronic degrees of freedom of a molecule.

An accurate description of electronic wave packet dynamics is essential for understanding and controlling ultrafast electron transfer and for applying it to control of chemical reactions. To our knowledge, there is no explicit and practical method for evaluating electronic wave packets of even two-electron molecular systems, because of difficulties arising from both singularities and long-range interaction in Coulomb potentials of a molecule. Recently, we have developed a new method for evaluating accurate propagation of an electronic wave packet.[35–37] We have called this the dual transformation method. In this method, both the electronic wave function and Hamiltonian are consistently transformed to overcome such difficulties. The dual transformation method is a powerful tool for analyzing the mechanisms of various related phenomena in intense fields, such as above-threshold ionization (ATI),[38,39] tunnel ionization,[38–42] enhanced ionization[43,44] and Coulomb explosion of molecules.[45–48]

In section 3, we present applications of this method to small molecular systems such as H_2^+ and H_2. In H_2^+, both the electronic and nuclear coordinates are treated quantum mechanically without using the Born–Oppenheimer approximation, an assumption of separation of electronic and nuclear motions in a molecule. To the best of our knowledge, the treatment of H_2 is the first accurate evaluation of two-electron dynamics of a

molecule. The results of these simulations provide a basis of the theoretical background of attosecond chemistry that will play an important role in the new research field of chemical reaction dynamics. We also propose an approach to evaluation of the electronic dynamics of multi-electron systems such as CO_2.

In the final section, we present a review on the quantum control of chemical reaction dynamics

1. Quantum Control of Nuclear Dynamics

We have developed two kinds of control theory based on local control theory.[18–20,25] In the early stage of our work, we developed a theoretical method based on the control theory of a linearly time-invariant (LTI) system, by which both the total population of the nontarget states and the total energies of the laser fields are minimized.[18–20] The optimization procedure consists of operation of the feedback gain matrix to the time-dependent state vector. This procedure is carried out at each successive short stage, in which the time-dependent Schrödinger equation can be approximated to the equation of motion of the LTI system.

Recently, we have developed another local control method that is based on the tracking problem.[25] In this subsection, we present an outline of this control method. Consider a molecular system interacting with a pulsed laser field $\varepsilon(t)$. The total Hamiltonian H(t) is given within the semiclassical treatment of the molecule-laser field interaction as

$$H(t) = H_0 - \mu\cdot\varepsilon(t). \tag{1}$$

Here, H_0 is the molecular Hamiltonian, and the second term is the interaction between molecules and the laser field in the dipole approximation, where μ is the dipole moment of the system. Time evolution of the system is determined by the time-dependent Schrödinger equation, given as

$$i\hbar\frac{\partial}{\partial t}|\Psi(t)\rangle = H(t)|\Psi(t)\rangle. \tag{2}$$

Here, $\Psi(t)$ is the solution of the time-dependent Schrödinger equation with the initial condition $\Psi(0)$ at $t = 0$.

We now consider a target operator, W, whose expectation value has a maximum value when the system reaches the objective state. The optimal control pulse is designed to maximize the expectation value of the target operator at the final time t_f, $\langle W(t_f)\rangle$, while minimizing pulse fluence. Then the objective functional, $J[\varepsilon(t)]$, to be maximized is defined as

$$J[\varepsilon(t)] = < W(t_f) > - \int_0^{t_f}\frac{dt}{\hbar A(t)}\,\varepsilon^2(t). \tag{3}$$

Here, the second term represents the cost penalty for the laser pulses with a time-dependent weighting factor , $A(t)$, with a positive value.

Let us now rewrite Eq. 3 as

$$J[\varepsilon(t)] = \int_0^{t_f} dt\left\{\frac{d}{dt}< W(t) > - \frac{\varepsilon^2(t)}{\hbar A(t)}\right\} + < W(0) > . \tag{4}$$

If we consider a special case in which the integrant in Eq. 4 is given by

$$\frac{d}{dt}< W(t) > - \frac{\varepsilon^2(t)}{\hbar A(t)} = g(t), \tag{5}$$

where $g(t)$ is a *known function of time*, the objective functional is expressed as

$$J[\varepsilon(t)] = \int_0^{t_f} dt g(t) + < W(0) > . \tag{6}$$

Since the right-hand side of Eq. 6 is constant, the pulse satisfying Eq. 5 leads to $\delta J = 0$, and such a pulse can be a candidate for the solution to the optimal control problem. The function $g(t)$ is regarded as a given trace in the tracking problem. From this viewpoint, we call the pulse derived from Eq. 5 a locally designed optimal pulse. Here "locally" means that the pulse determined by Eq. 5 at each time between 0 and t_f is a solution of the control problem.

The expression of the locally optimized pulse is derived by evaluating

$$\frac{d}{dt}< W(t) >$$

in Eq. 5 as

$$\begin{aligned}&\varepsilon(t)^2 - iA(t)\langle\psi(t)|[W,\mu]|\psi(t)\rangle\varepsilon(t)\\ &+ iA(t)\langle\psi(t)|[W,H_0]|\psi(t)\rangle + \hbar A(t)g(t) = 0,\end{aligned} \tag{7}$$

in which [,] represents the commutator such that $[W,\mu] = W\mu - \mu W$.

If we consider a special tracking path of $g(t) = 0$, then we have the equation of the local control pulse as

$$\begin{aligned}&\varepsilon(t)^2 - iA(t)\langle\psi(t)|[W,\mu]|\psi(t)\rangle\varepsilon(t)\\ &+ iA(t)\langle\psi(t)|[W,H_0]|\psi(t)\rangle = 0.\end{aligned} \tag{8}$$

Since the path of $g(t) = 0$ requires a trivial solution of $\varepsilon(t) = 0$, the target operator should commute with the molecular Hamiltonian,

$$[W,H_0] = 0. \tag{9}$$

Another solution associated with the path of $g(t) = 0$ gives the expression of the local control pulse as

$$\varepsilon(t) = -2A(t)\,\mathrm{Im}\langle\psi(t)|W\mu|\psi(t)\rangle. \tag{10}$$

It can be easily shown from Eq. 5 that the condition $g(t) = 0$ satisfies

$$\frac{d}{dt}< W(t) > = \frac{\varepsilon(t)^2}{\hbar A(t)} \geq 0. \tag{11}$$

The above equation means that the value of $\langle W(t)\rangle$ increases in proportion to the pulse energy. In other words, the system goes towards its target because the objective state gives the maximum value to $\langle W(t)\rangle$ at each time by applying the local control pulse.

The commutation relation, Eq. 9, seems to exclude non-stationary targets in the treatment of wave packet control. This restriction can, however, be removed by calculating the control pulse backward in time.[27] Starting with a final non-stationary state, the pulse is designed to transfer the molecule into a stationary initial state. The validity of this backward time-propagation method is guaranteed by the time reversibility of the Schrödinger equation. We can, thus, apply Eq. 10 to the control of any target as long as molecules are initially in a stationary state or in thermal equilibrium [see Sec. 2.4].

So far we have presented a local optimization method for obtaining pulses for control of chemical reaction dynamics. There is another control method, called the global optimization method.[9,10,15] The optimal pulse can be obtained by solving the time-dependent Schrödinger equation iteratively with both initial and final boundary conditions. That is, the time-dependent Schrödinger equation is solved for both the forward and the backward propagation of the reaction system. By using this method, one can search the true optimal solution of the reaction system in the presence of many local solutions. Convergence problems sometimes arise when global optimization method is used. Compared with the global optimization method, the local control method has a simple algorithm, that is, only one-sided propagation is needed as described above, and there is no convergence problem. However, one should always note that the solution is a local one.

2. Application

2.1 Photo-Isomerization. Photo-isomerization of organic molecules such as *cis–trans* isomerization of butadiene and stilbene is one of the typical chemical reactions induced by visible lights or UV light.[49,50] *cis–trans* Isomerization plays an important role in the primary photo-processes in the light-driven transmembrane proton pump bacteriorhodopsin.[51] As the first application of the local control method described in the preceeding section, we consider a photo-isomerization of a one-dimensional model molecule that consists of two electronic states (g and e).[52] Figure 1 shows the model potential energy surface (PES) whose parameters are given in Ref. 52. The ground electronic state has two wells that correspond to two isomers, called isomer A (left well) and isomer B (right well). Isomer A is assumed to be the initial state. The middle barrier separates these isomers, since the tunneling interaction is weak. Our objective is to design a pulse that creates isomer B by controlling a wave packet motion on the excited PES. In our control treatment, the wave function is expanded in terms of vibrational eigenstates in both PES's. The time evolution of the wave function is calculated by the Runge–Kutta method. The transition moment is assumed to be coordinate-independent and to have a magnitude of 1.0 D. Because of Eq. 9, the target operator must have a form of

$$W = \sum_{\mathrm{v}} \{|gv\rangle w_{gv}\langle gv| + |e\mathrm{v}\rangle w_{ev}\langle ev|\}, \qquad (12)$$

where $|gv\rangle$ and $|ev\rangle$ denote vibronic states in the ground and excited electronic states, respectively, and the weight factors $\{w_{gv}\}$ and $\{w_{ev}\}$ allow for flexibility in choosing the relative importance of the physical objectives. Since the control pulse designed by the local control procedure monotonically increases the target expectation value, here we choose $w_{gv} = 0$ ($\mathrm{v} \neq 2$), $w_{ev} = 0.3$ and $w_{gv=2} = 1.0$ in order to transfer isomer A to the lowest state of isomer B, $|gv = 2\rangle$ through the excited electronic state.

Figure 2a shows the control pulse and populations as a function of time. The population of isomer A (isomer B), $P_A(t)$ [$P_B(t)$], is given by summing the populations over the vibronic states, $v = 0$, 1, 3, 5 ($v = 2$, 4) in the ground electronic state. The numerical result clearly shows a pump–dump wave packet control, as described in the Introduction section. The electric field consists of a pump pulse and a few dump pulses. We would like to emphasize that we have not assumed any specific shape of control pulses or pulse separations. Our local feedback control method brings about such a pump-dump scenario.

The first pulse is a pump pulse that transfers almost 100% of the population to the excited PES and creates a wave packet on

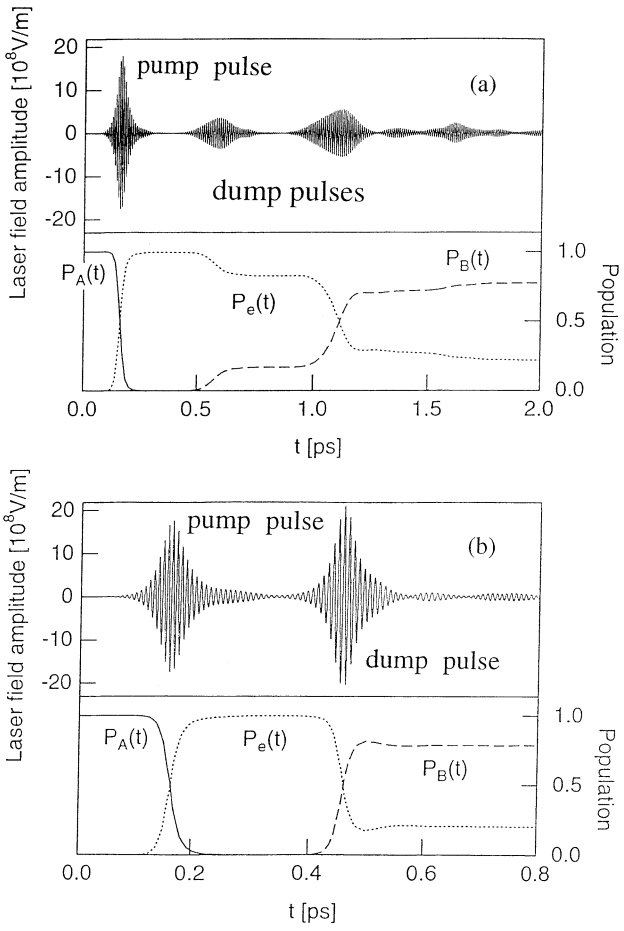

Fig. 2. Control pulse as a function of time (upper figure), and time evolution of the isomer A (isomer B) population, $P_A(t)$ [$P_B(t)$], and that of the excited electronic state, $P_e(t)$ (lower figure) in the cases of the control time $t_f = 2.0$ ps (Fig. 2a) and $t_f = 800$ fs (Fig. 2b). [from Ref. 52]

the electronically excited state. Then two dump pulses whose timing is in accord with this wave packet motion appear. That is, when the packet reaches the Franck–Condon region of the $|gv = 2\rangle$ state, the dump pulses induce a transition to this target state. We can see that within 2.0 ps, about 80% of the population is transferred to the right well, which consists only of the $|gv = 2\rangle$ state. The remaining 20% of the population is distributed among vibrational states on the excited PES that have small Franck–Condon factors with the target state.

To complete the control within a shorter time scale, say 800 fs, we must design a stronger dump pulse. For this purpose, we then choose a weight factor of $w_{gv=2} = 3.0$ that is larger than that in Fig. 2a, while the other weight factors are the same as before. The calculated control pulse and time-evolution of populations are shown in Fig. 2b. The dump pulse has a sufficiently high intensity to complete the dumping process by one pulse. Thus, the whole control pulse consists of a pair of pump and dump pulses. This pair of pulses transfers about 80% of the population to the right well (corresponding to isomer B). It is interesting to compare the vibrational components of the final state in the two cases. In the case of Fig. 2b, about 15% of the population is in the vibrationally excited state, $|gv = 4\rangle$. In other words, a hot isomer B is produced by using such an intense dump pulse. This is because the temporal width of the dump pulse is too short for it to be able to energetically resolve the vibrational state in the right well.

The above numerical results indicate that a pump–dump-type excitation scheme is an efficient control method for achieving photo-isomerization within short time regimes. It is also possible to apply the local control method to cases in which control time is long enough to resolve the vibrational energy spacing of the vibronic states. Although we do not show the numerical results, our local control method predicts an optimal pulse that connects the initial and the objective state through one vibronic state that has the most favorable Franck–Condon for both the excitation and deexcitation processes.

We have used a simple one-dimensional model to demonstrate the applicablity of our control method to photo-isomerization. For actual systems, we have to take into account multidimensional effects of the PES's. One of the main effects is rapid intramolecular vibrational energy redistribution (IVR) processes between the reaction and interaction modes. One solution to avoid these undesirable effects is to complete the control before the IVR processes affect quantum control. Ultrashort pulse control described here may be an effective scheme for this purpose.

2.2 Predissociation of Sodium Iodide. Sodium iodide (NaI) is one of the molecules that have attracted the interest of many experimental as well as theoretical researchers from the viewpoint of quantum control.[53–59] It is well known that the ground ionic state potential crosses an excited state potential characterized by covalent nature around internuclear distance R = 6.9 Å as shown in Fig. 3. The nonadiabatic coupling induces predissociation. Study of this system has been stimulated by the pioneering works by Zewail's group[58] who directly observed the predissociation dynamics using ultrafast laser techniques. Calculations of wave packet dynamics of this system have been reported. As for quantum control of NaI, for example, Herek et al.[59] controlled the branching ratio between

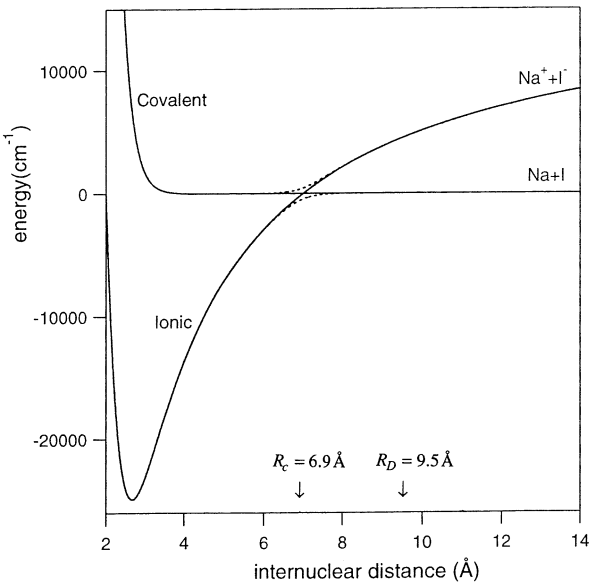

Fig. 3. Model potential energy surfaces (PES's) for NaI, whose parameters are taken from Ref. 60. The solid (dotted) line shows the diabatic (adiabatic) PES's. [from Ref. 28]

two channels of photodissociation products by adjusting the time delay between the pump and clock pulses. In this experiment, the frequency of the clock pulse is chosen to specify the position at which the wave packet is excited to one of the product channels. Use of a narrow spatial distribution of the wave packet can control branching ratios Na*/Na. Based on this idea, Wilson's group created a spatially localized wave packet by using a negatively chirped pulse.[56] Although their numerical simulation showed that this chirped pulse increased the selectivity at 0 K, this effect was considerably diminished by thermal distribution at 1000 K, and the latter result was confirmed experimentally.

On the other hand, we investigated several optimized control schemes to accelerate the predissociation of NaI. We present several scenarios based on the local control method[26–27], including a pump-dump-type control[26] and a wave packet-shaping-based method.[27] Here, NaI is modeled by a one-dimensional, two-electronic-state system, as shown in Fig. 3. The model consists of ionic ground and covalent excited states with the potential parameters in Ref. 60. The time-evolution of a wave function is numerically solved by the split operator + FFT (fast Fourier transform) scheme. The potential couplings due to non-adiabatic interaction and optical transitions in the split operator are represented in terms of the 2×2 Pauli matrices.

Pump-Dump Control Scheme. In our previous paper,[55] we showed that the predissociation of NaI could be controlled by applying a linearly positive-chirped pump pulse without using optimization theory. The goal of our previous study was to produce as much neutral photodissociation products of NaI as possible within one cycle of nuclear vibration. Here we present the design of a control pulse to achieve the same purpose based on the local control method.[25] The target operator is chosen as

$$W = |i_0\rangle\, w_i\, \langle i_0| + \int_{R_D}^{\infty} dR\, |cR\rangle\, w_d\, \langle cR|, \tag{13}$$

where $|i_0\rangle$ is the lowest vibrational state in the ground ionic state, and $|cR\rangle$ is a covalent state at a nuclear distance R (in the diabatic representation). In Eq. 14, the first term is associated with the pumping process, in which a weight w_i has a negative value to generate a pump pulse. The second term with a positive weight, w_d, is introduced to induce the dumping process. The domain of the integration is specified by $R_D = 9.5$ Å, since wave packet components going beyond this point are regarded as dissociation products.

The locally designed pulse as a function of time is given in Fig. 4a, in which the two temporal peaks correspond to pump and dump pulses. The first pulse (pump pulse) has a maximum field strength of 6×10^9 V m^{-1}, which corresponds to a peak intensity of 4.8 TW cm^{-2}. The inset shows the time- and frequency-resolved spectrum of the second pulse. We can see that the central frequency of the dump pulse increases almost linearly in time. (A straight line is drawn in the figure as a guide.) Thus, the pulse is approximated by a positive-chirped pulse, which agrees with the results of our previous analysis.[55] The feature originates from the coordinate dependence of the energy difference between the two electronic states. Beyond the crossing point of the potentials, the energy difference increases almost linearly with internuclear distance, resulting in an increase in transition frequency. The important role of chirped pulses in controlling nuclear dynamics was demonstrated by other groups as well.[61–63]

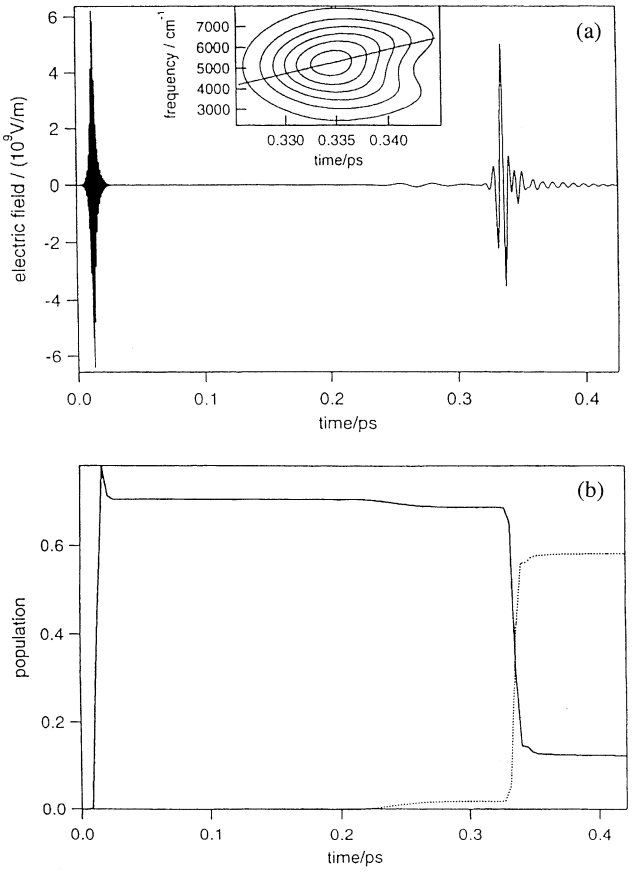

Fig. 4. (a) Control pulse as a function of time, and the time- and frequency-resolved spectrum of the dump pulse (inset).
(b) Time evolution of populations. The solid line shows the time-evolution of thepopulation in the excited adiabatic PES, and the dotted line shows that of the photodissociation product. [from Ref. 27]

The time evolution of populations is shown in Fig. 4b. The solid and the dotted line denote the population in the excited state (adiabatic representation) and that of dissociation components, respectively. About 80% of the population is transferred into the excited state by the pump pulse, and finally about a 60% yield of photodissociation is produced by the controlled dump pulse within one cycle of NaI stretch vibration. Before the dump pulse, we see a small increase in the dissociation component. This is attributed to spontaneous predissociation due to the non-adiabatic coupling between the excited and ground adiabatic states.

Figure 5 shows the time evolution of the absolute value of the wave packet on the ionic PES in the diabatic representation. Around the equilibrium internuclear distance, we can see oscillating components that are created by the stimulated emission during the pumping process. This vibrational coherence will be utilized in the control scenario described in the next subsection. The excited wave packet is initially created on the covalent diabatic state and then moves to the ionic state, which is the component appearing around R $\sim$ 7 Å. This wave packet is transferred to the dissociative covalent state by the linearly chirped dump pulse. In Fig. 5, this corresponds to the sudden disappearance of the ionic wave packet at R $\sim$ 10 Å.

Wave Packet-Shaping Scheme. To get a basic idea of the control based on wave packet shaping, we first consider the excited population and the normalized dissociation probability when NaI is excited by a short (60 fs) intense Gaussian pulse. The normalized dissociation probability is defined as the dissociation product created within the first half period of the wave packet oscillation, which is then normalized with respect to the amount of the excited population. The pulse has a peak intensity of 3×10^9 V m^{-1}, while it has a variable central frequency changing from 28000 cm^{-1} to 38000 cm^{-1}.

Figure 6 shows the amount of excited population and nor-

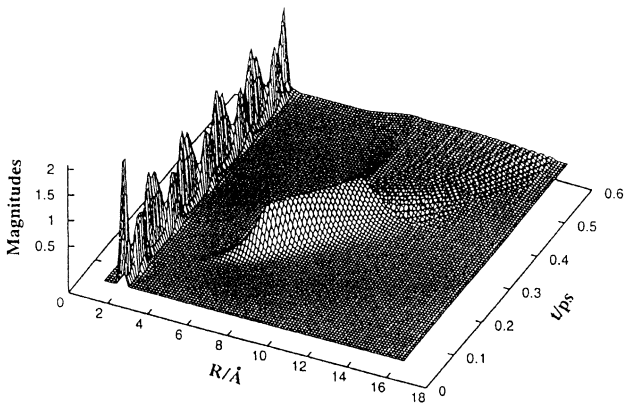

Fig. 5. Time evolution of the nuclear wave packet on the ionic diabatic state. [from Ref. 27]

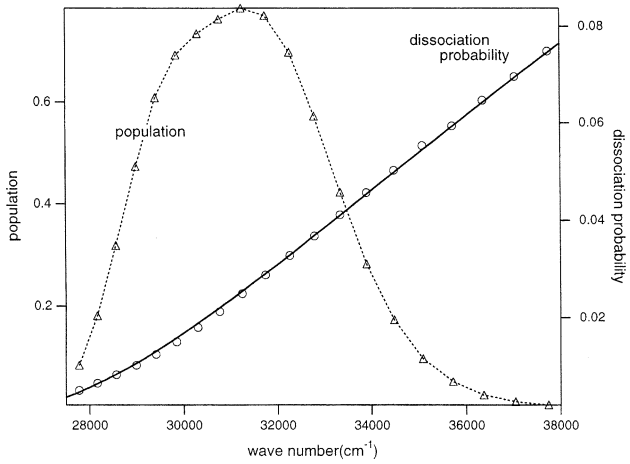

Fig. 6. The excited population (triangles with a dotted line) created by an ordinary, uncontrolled Gaussian pulse and the normalized dissociation probability (circles) as a function of a central frequency of the Gaussian pulse. The solid line shows the least-squares fitting with the Landau–Zener formula. [from Ref. 28]

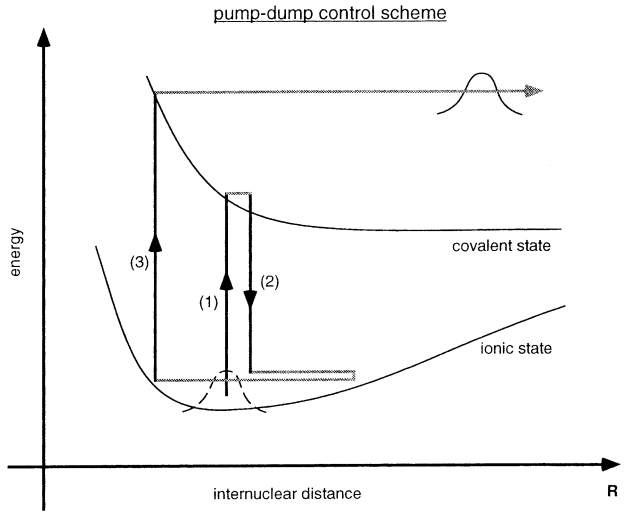

Fig. 7. Schematic illustration of a modified pump–dump control. The first pump (1), dump(2) and the second pump (3) processes are indicated by solid lines. [from Ref. 28]

malized dissociation probability as a function of frequency. The excited population profile reflects the distribution of Franck–Condon factors between the lowest (initial) state and the excited vibronic states. The peak frequency around 31200 cm^{-1} corresponds to the absorption maximum. On the other hand, the normalized dissociation probability increases as frequency increases. This can be explanied by the Landau–Zener mechanism, i.e., a wave packet with a higher velocity can cause non-adiabatic transitions more efficiently and can accelerate predissociation. To create such a wave packet with a high velocity, however, we have to overcome difficulties originating from the restriction due to the Franck–Condon overlap relevant to optical transitions.

From the above consideration, we adopt the modified pump–dump excitation scheme as illustrated in Fig. 7. The

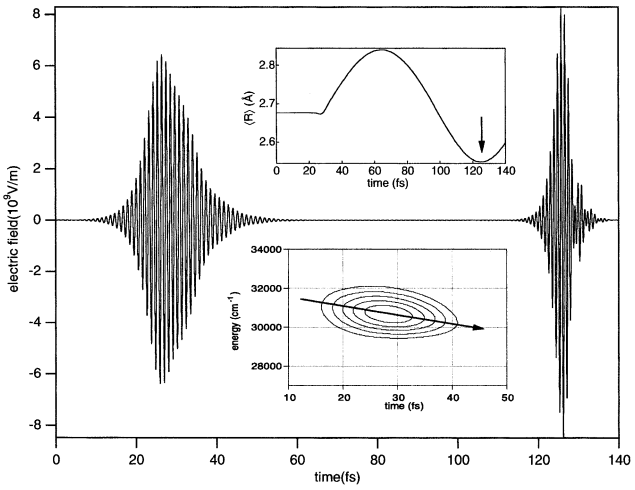

Fig. 8. Control pulse as a function of time. The upper inset shows the average position of the wave packet that is created by the intra-pulse pump–dump process. The lower inset shows time- and frequency-resolved spectrum of the first pulse in which the arrow indicates the linear frequency change as time. [from Ref. 28]

first pump pulse (pulse 1) creates a wave packet on the excited PES. This excited packet moves down to the PES and reaches another Franck–Condon region, which is a favorable region to create a wave packet with a large amplitude in the ground state PES. A dump pulse (pulse 2) induces this second process. The packet oscillates within the ground PES until it reaches the inner turning point, at which the packet is pumped up to the excited PES again by a second pump pulse (pulse 3).

According to this scenario, we construct a target operator and calculate a local control pulse. Figure 8 shows the designed pulse. This is not a simple series of three subsequent pump and dump pulses, as suggested in Fig. 7. The first pulse around $t \sim 25$ fs creates a wave packet within the ground PES through an intra-pulse pump–dump mechanism. The second pulse around $t \sim 128$ fs then transfers this packet to the excited state. The time lag between these pulses is determined by the timing at which the packet on the ground PES reaches the inner turning point, as shown in the inset of Fig. 8. Comparing the normalized dissociation probabilities, the local control pulse, for example, gives a 2.84-times larger probability than a 60 fs Gaussian pulse whose central frequency is tuned to the absorption maximum. The control pulse can transfer a large amount of the population to the excited state. The wave packet created on the excited state has a high kinetic energy at the potential crossing to enhance the predissociation.

In our calculation, the intra-pulse pump–dump mechanism was predicted by the local control method. Note that, except for introducing a specific target operator for our purpose, we have not employed any physical intuitions to design the control pulse. To analyze the features of the pulse, we obtain a time- and frequency-resolved spectrum, which is shown in the inset of Fig. 8. We can see a negatively chirped pulse whose structure can be understood on the basis of the semi-classical description of wave packet dynamics. If the Newton equation is applied to estimation of the velocity of the wave packet in the covalent state, the gained kinetic energy is estimated as $\Delta T =$

550 cm^{-1} at $t = 5$ fs that corresponds to the temporal duration of an intra-pulse pump–dump process. The numerical result shows that the wave packet created by the control pulse has a $\Delta T = 530$ cm^{-1} higher average vibrational energy than the initial state. This increase in energy is in good agreement with the estimated value. Since our system has a steep slope around the Franck–Condon region, the intra-pulse excitation mechanism is efficient in generating a wave packet with a large amplitude in the ground PES.

Experimentally, the importance of the intra-pulse pump–dump excitation has been demonstrated by Shank's group using dye molecules.[64,65] Since we saw the same mechanism in a very different system, the intra-pulse pump–dump excitation mechanism can be regarded as a useful excitation technique for controlling molecular dynamics. This has also been pointed out by Cao, Wilson and co-workers.[66,67] Recently, they proposed a new population inversion scheme (which they called a molecular pi-pulse) that combines a positive chirping with an adiabatic rapid passage.

If we are concerned with a longer time scale, e.g., a few picoseconds, the control scheme based on the Landau–Zener mechanism does not always give an efficient means for accelerating predissociation. This is because a wave packet with a higher vibrational energy has a longer oscillation period and, thus, has fewer chances to pass the crossing point. To control predissociation within a few picoseconds, we adopt another control scheme that consists of two steps. In the first step, we determine the target packet that has the shortest lifetime within a given time interval, $[t_0, t_f]$. Since this packet gives the maximum product yield, in the second step, we design a control pulse that creates this target packet at time t_0.

The target packet is obtained so as to minimize the survival probability, S, defined below. If we assume that a target packet, $|\psi_T\rangle$, is prepared at time t_0, then the bound components of the packet at time t_f is expressed as

$$S = \frac{\langle \Psi_T | U_0^{\dagger}(t_f,t_0) B U_0(t_f,t_0) | \Psi_T \rangle}{\langle \Psi_T | \Psi_T \rangle}. \tag{14}$$

Here, $U_0(t_f, t_0)$ is a free propagator that is presented by the molecular Hamiltonian without optical interactions. In the adiabatic representation, the projector for the bound components, B, extracts all the bound components on the excited ones. Since the target packet should be generated by a control pulse, it must be optically connected with the initial state. This leads to the constraint that the target packet is within a subspace of optically accessible states, specified by a projection operator, P:

$$P|\psi_T\rangle = |\psi_T\rangle. \tag{15}$$

Using a conventional variational procedure under this constraint, we can derive the eigenvalue equation that the target packet satisfies:

$$PU_0^{\dagger}(t_f, t_0) B U_0(t_f, t_0) P|\psi_T\rangle = \lambda P|\psi_T\rangle. \tag{16}$$

The eigenstate with the minimum eigenvalue, i.e., the shortest lifetime, is our target packet. We expand the target packet in terms of the vibrational states in the excited adiabatic PES and then solve Eq. 16 by a diagonalization method.

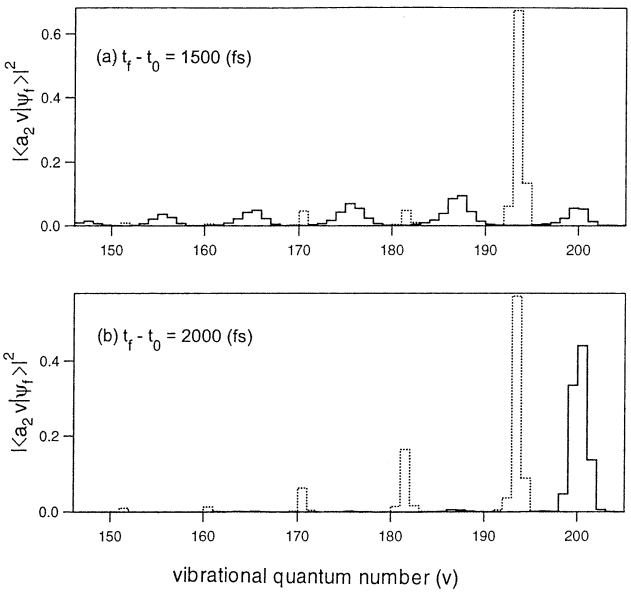

Fig. 9. Vibrational distribution of the target packets for time intervals, (a) $t_f - t_0 = 1500$ fs and (b) 2000 fs. Those of the wave packets with the largest survival probabilities are shown by dotted lines for reference. [from Ref. 28]. The basis $|a_2 v\rangle$ represents the v-th vibrational state in the excited adiabatic state.

If we choose $t_f - t_0 = 1500$ fs, then the target packet has an eigenvalue of $\lambda = 0.859$, which means that 14.1% of the population dissociates after 1500 fs. Figure 9 shows vibrational distributions of the target packet with the minimum eigenvalue (solid line) for two time intervals: $t_f - t_0 = 1500$ and 2000 fs. For reference, the packet with the largest eigenvalue (the longest lifetime) is shown by a dotted line in each figure. We can see that the packet with the minimum eigenvalue shows an opposite distribution pattern to that with the largest one. This is because the packet with the shortest (longest) lifetime consists of vibrational states with a short (long) lifetime. Another characteristic is that the packet with the largest survival probability tends to include higher vibrational states, since such states have a longer oscillation period and can reduce the chances of passing the crossing point.

In the second step, the local control pulse that creates the non-stationary target is calculated using Eq. 11. Since the local control procedure requires that the physical objective should be represented by a stationary target operator in the sense of Eq. 9, as mentioned in Sec.1, the pulse is designed by the backward time propagation. That is, the pulse design starts with the target packet to create the initial states. Because of the time-reversibility of the Schrödinger equation, when the calculated pulse is substituted back into the Schrödinger equation for forward propagation, the pulse can produce the same control yield as that obtained in backward calculation.[25] Figure 10a shows the control pulse as a function of time, and Fig. 10b shows its time- and frequency-resolved spectrum in the case of $t_f - t_0 = 1500$ fs. At time t_0, the pulse produces quite a high control yield, in which the absolute square of the overlap

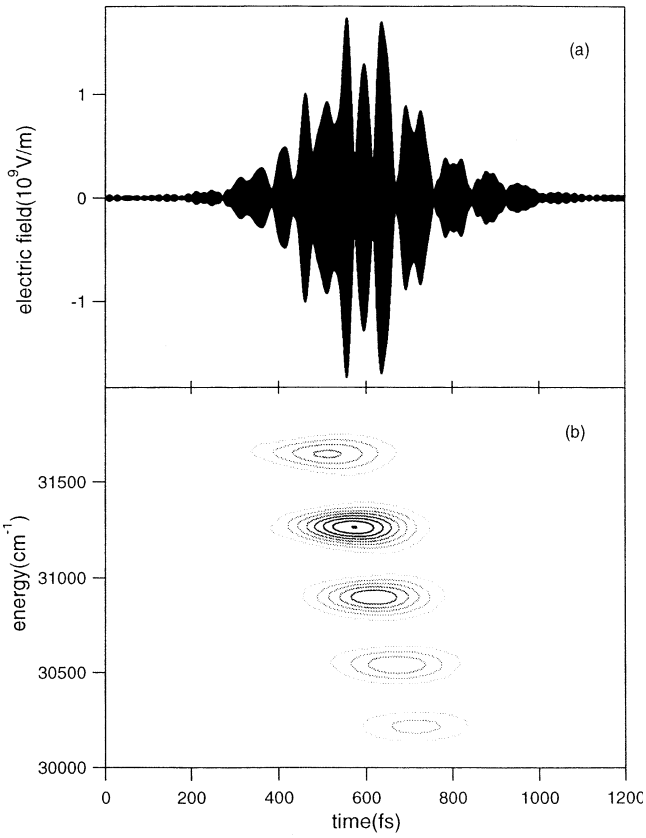

Fig. 10. Control pulse for shaping the target packet in Fig. 9a. (a) The control pulse as a function of time, and (b) its time- and frequency-resolved spectrum. [from Ref. 28]

between the target and the optically prepared packets is 0.982. We see from Fig. 10b that the pulse consists of five frequency components, which correspond to five distribution peaks in Fig. 9a. Reflecting the differences in oscillating periods, each frequency component has a slightly different temporal peak. That is, the wave packet components consisting of high vibrational states take a longer time to reach the crossing than do those of low vibrational states. This can explain the structure of the spectrum in Fig. 10b. We can also design a control pulse that generates a packet with the longest lifetime and obtain almost the same control yield, although we do not show the numerical results here. Thus, the two-step control scenario works well for calculation of control pulses that efficiently accelerate the predissociation in a few-picosecond time regimes.

2.3 Quantum Control of Dark States. In general, in a polyatomic molecule, a nuclear wave packet created by a laser pulse is destroyed by various dephasing processes, including intramolecular vibrational energy redistribution (IVR) processes caused by intramolecular vibrational interactions such as anharmonic coupling or kinetic-energy coupling.[68–70] Due to IVR, the initial optical excitation is transferred into other states that are not optically connected directly with the ground state. Since these dark excitations are spread over many vibrational degrees of freedom, the IVR processes are usually regarded as enemies for control. From a different viewpoint, however, IVR processes offer a method to create a tailored dark excitation. If an appropriate dark state can be prepared, it is possible to induce new photochemical dynamics. According to this scenario, we aim at creating a target wave packet, especially a dark packet, at a specified time.

As a case study, we consider a two-dimensional vibrational system that models the interaction of a CH stretch with an adjacent CCH bend in a CH overtone excitation process of a polyatomic molecule in the ground electronic state. We assume the same Hamiltonian as that in Ref. 71, in which the stretch (bend) is approximated by a Morse (harmonic) oscillator. This qualitative model can describe subpicosecond energy exchange processes between the two modes, although it is of limited value for quantitative analysis of IVR.

The molecular Hamiltonian is composed of three parts: the zero-order Hamiltonian of the stretch, $H_0^{(S)}$, that of the bend, $H_0^{(B)}$, and the kinetic coupling between them, $V^{(SB)}$.[21] The interaction originates from the difference between instantaneous and equilibrium bond lengths. A vibrational eigenstate is represented as a linear combination of the zero-order states $\{|v_S, v_B\rangle\}$ by a diagonalization method, in which v_S (v_B) denotes the quantum number of the stretch (bend). In the following numerical illustrations, we set a pure bend state, $|0, 8\rangle$, as a target. Since one quantum of the stretch is close in energy to two quanta of the bend, we take into account $|0, 8\rangle$, $|1, 6\rangle$, $|2, 4\rangle$, $|3, 2\rangle$ and $|4, 0\rangle$ states to obtain the eigenstates belonging to this IVR manifold. The other states are neglected because of large energy separation. We assume that the molecule is initially in the lowest state, $|0, 0\rangle$. Figure 11 illustrates the level structure and optical interactions of our system. Concerning the optical transition moments, it is a good approximation to consider that only the $|4, 0\rangle$ is optically connected with the $|0, 0\rangle$. We further assume an artificially large value of the transition moment, 1.0 D, for this transition, since we are interested in qualitative analysis of the control mechanism. Thus, the overlap integral between the $|4, 0\rangle$ state and each eigenstate gives the transition moment matrix element if we read it in units of Debyes.

Our goal here is to design a control pulse that transfers the initial population into a large amplitude bending, dark state, $|0, 8\rangle$. Special attention is given to the dependence of the control achievement on the choice of a final time, t_f. The calculated pulses when the final times are set to t_f = 500 and 100 fs are shown in Figs. 12 and 13, respectively. Each figure shows (a) the control pulse as a function of time, (b) time-evolution of populations, and (c) a trajectory in a quantum number space. The quantum number space has two axes, one that denotes the average quantum number of the stretching mode and one that denotes the bending mode. These averages, $\langle v_S(t)\rangle$ and $\langle v_B(t)\rangle$, are defined as

$$< v_S(t) > = \sum_{j=0,2,4,6} (4 - j/2) |\langle 4 - j/2, j|\Psi(t)\rangle|^2 \qquad (17a)$$

and

$$< v_B(t) > = \sum_{j=2,4,6,8} j |\langle 4 - j/2, j|\Psi(t)\rangle|^2, \qquad (17b)$$

where $|\psi(t)\rangle$ is a wave function at time t. The IVR processes due to the 2:1 Fermi resonance are denoted by a straight line with a gradient of -2 in the average quantum number space. The trajectory starts at the origin and reaches the point (0, 8)

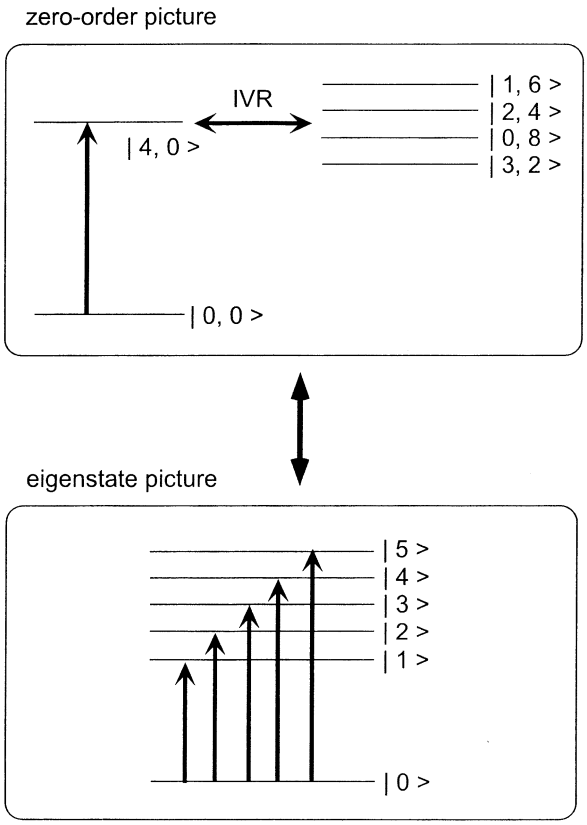

Fig. 11. Level structure of the model in the zero-order picture (upper figure) and that in the eigenstate picture (lower figure). The vertical arrows indicate optically allowed transitions. [from Ref. 21]

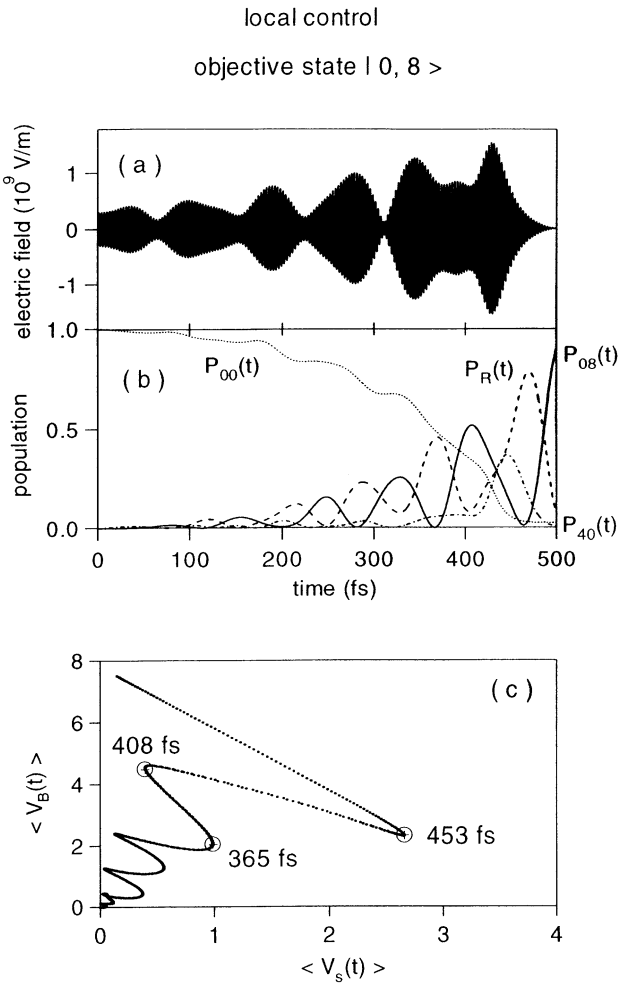

Fig. 12. (a) Control pulse as a function of time in the case of t_f = 500 fs. (b) Time evolution of the population, $P_{mn}(t)$, for a zero-order state, $|m, n\rangle$; $P_{00}(t)$ (dotted line), $P_{40}(t)$ (dot-dashed line), $P_{08}(t)$ (solid line), and $P_R(t) = 1 - P_{00}(t) - P_{08}(t) - P_{40}(t)$ (dashed line). (c) Trajectory plot in the quantum-number space. $\langle v_S(t)\rangle$ and $\langle v_B(t)\rangle$ are the average quantum number of the stretching mode and that of the bending mode. [from Ref. 21]

when the control is perfect. The trajectory plot can help us to understand the control mechanism.

The numerical results in the case of t_f = 500 fs are given in Fig. 12. About 90% of the population is transferred to the target state in this case. The pulse design algorithm adjusts the pulse frequency, intensity and phase to actively control the IVR processes. For example, comparing Fig. 12a with b, we can see a correlation between the modulation pattern of the pulse and the time-evolution of the $|4, 0\rangle$ population, although the optically prepared $|4, 0\rangle$ is spread into other states so quickly that only a small amount of population is found in this state, except at t $\sim$ 450 fs. This feature is clearly shown in the trajectory plot in Fig. 12c. Before $t \sim$ 410 fs, the average quantum number of the stretch always has a value of less than 1. The wave packet created by the last peak around $t \sim$ 410 fs constructively interferes (t_f = 500 fs) with the previously prepared components to generate the target $|0, 8\rangle$ state.

In Fig. 12a, the pulse after $t \sim$ 310 fs can be regarded as a core part, whereby most of the population is excited. It is known that a control pulse has a "core" structure that is essential to achieve an objective. The other parts of the control pulse before the core structure are used to adjust the phase relations of the eigenstates for the next control stage.

Figure 13 shows the results in the case of t_f = 100 fs. The pulse still selectively excites the target state, although about 50% of the population is in the initial state at the final time. This is mainly due to the fact that t_f = 100 fs is too short even for the construction of the core structure of the control pulse. The limitation of control originates from the lack of energy selectivity due to a short control time. In fact, the shortest time required for control is estimated as 150 fs from the energy spacings of the eigenstates, which is longer than the present control time of t_f = 100 fs.

2.4 Selective Preparation of Enantiomers from Racemate. Recently, selective preparation of enantiomers from racemates using light has attracted much attention from the viewpoint of establishment of a new synthetic scenario as well as determination of the origin of chirality of amino acids.[72,73] New scenarios based on quantum control have been proposed.[29,74–79] In this section, we outline a quantum control of selective preparation of enantiomers from racemates at low temperature. We use a theoretical treatment of quantum control in density matrix formalism.[19,29,80–83]

Two fundamental issues concerning quantum control of enantiomer preparation from a racemic mixture should be de-

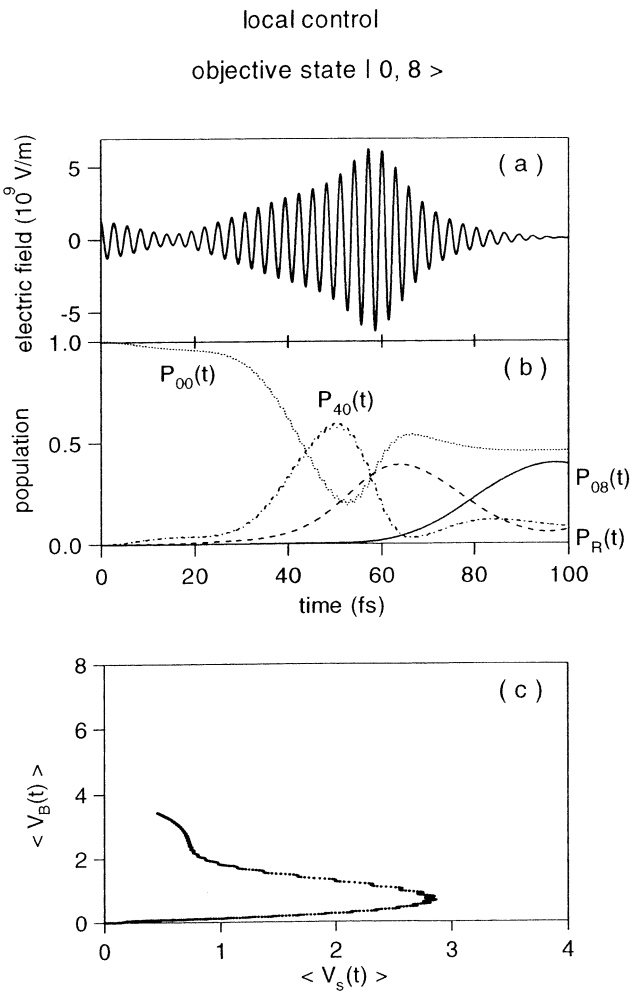

Fig. 13. The same as those in Fig. 12 except that the final time is chosen as $t_f = 100$ fs. [from Ref. 21]

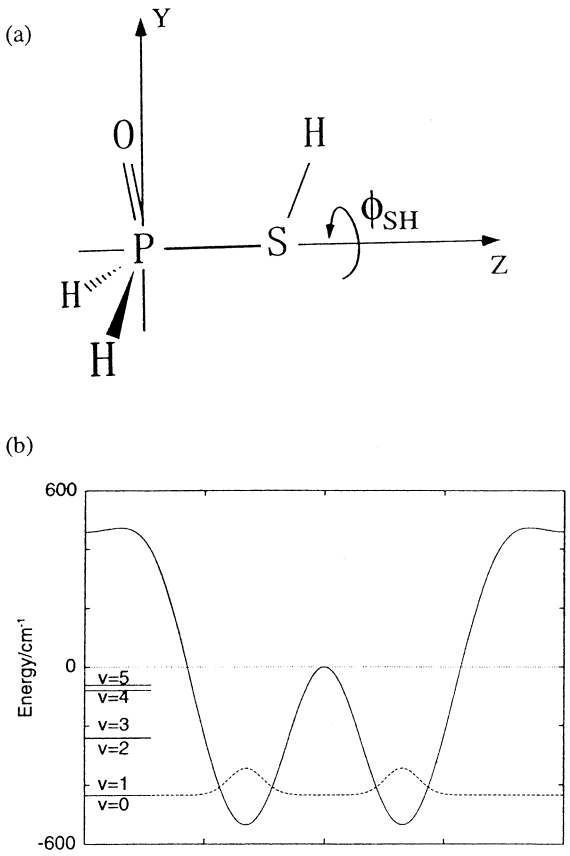

Fig. 14. (a) Geometry of H_2POSH in a one-dimensional model. [from Ref. 29]. (b) The double well potential function and several eigenvalues ($v = 0, 1, ..., 5$. The eigenfunction of the lowest state is shown by a dotted line as well. [from Ref. 77]

scribed here.[29] The first issue is that an isotropic ensemble, such as that in a gas phase or in homogeneous solvents, can not be controlled within dipole approximation as is usually adopted in ordinary quantum control. Therefore, it is necessary to introduce asymmetry into the ensemble of racemates by, for example, letting racemates be preoriented. The second issue is that complete enantiomer preparation in the ground vibrational state can not be performed in any mixed system without dissipative processes such as spontaneous emission. This restriction can be understood from the fact that the maximum value of the population transferred can not exceed the maximum value of the initial population distribution.

Preoriented phosphinotioic acid, H_2POSH, was used as a model system for several reasons. First, this molecule has elements essential to biological substances. Second, it is a simple molecule whose potential energies and dipole moments can be evaluated by an ab initio MO method.[77] We adopted a one-dimensional model of the molecule. In this model, the torsion of SH around the PS bond is the reaction coordinate, and its potential is characterized by a symmetric double well potential. This system has dynamic chirality because the localization time of a wave packet in one well is ~600 ps, i.e, due to tunneling, the wave packet created dephases with dephasing time of 600 ps. Such a system is not a chiral molecule as shown in Fig. 14, but it is called dynamic chirality.[84,85] We call the *L*-form of the molecule in the *L*-well and the *R*-form in the *R*-well. A selective preparation of enantiomers is carried out by using two linearly polarized pulses propagating along the space-fixed *Z* axis in Fig. 14, $\varepsilon_X(t)$ for the X component and $\varepsilon_Y(t)$ for the Y component. The locally optimized control fields derived in the density operator formalism are expressed as[28]

$$\varepsilon_X(t) = -2A\mathrm{Im}Tr\{\rho(t)W\mu_X\} \tag{18a}$$

and

$$\varepsilon_Y(t) = -2A\mathrm{Im}Tr\{\rho(t)W\mu_Y\}. \tag{18b}$$

Here, A that corresponds to a weighting factor in Eq. 3 is taken to be a positive constant for simplicity. $\rho(t)$ is the density operator of the system, and μ_X and μ_Y are the dipole moments of the X and Y components, respectively. The initial distribution $\rho(t_0)$ is assumed to be a Boltzmann distribution. We consider the system in a low temperature case in which the lowest state $|0+\rangle$ and the next-lowest state $|0-\rangle$ are approximately equally populated since their energy separation (0.05 cm^{-1}) is small. In this case, the initial density operator can be expressed in the eigen state basis set as

$$\rho(t_0) = \frac{1}{2}\{|0+\rangle\langle 0+| + |0-\rangle\langle 0-|\}. \quad (19)$$

The initial density operator can be transformed into the localized basis set, $|vR\rangle$ and $|vL\rangle$, as

$$\rho(t_0) = \frac{1}{2}\{|0R\rangle\langle 0R| + |0L\rangle\langle 0L|\}. \quad (20)$$

Here, v in front of $R(L)$ denotes the quantum number of the torsional mode.

We consider an enantiomer selection of *R*-form starting from an equal mixture of racemates in a low temperature limit case. The target operator is taken to be

$$W = \frac{1}{2}\{|0R\rangle\langle 0R| + |1R\rangle\langle 1R|\}. \quad (21)$$

Figure 15a shows the localization of enantiomers to R-from as a function of time. We can see that almost complete localization on the right-well is realized within 60 ps. The oscillating behavior in Fig. 15a, whose period is of 21 ps, is associated with the frequency difference between excited vibrational eigenstates, $|1+\rangle$ and $|1-\rangle$, which are coherently excited by optimal control pulses shown in Fig. 15b.

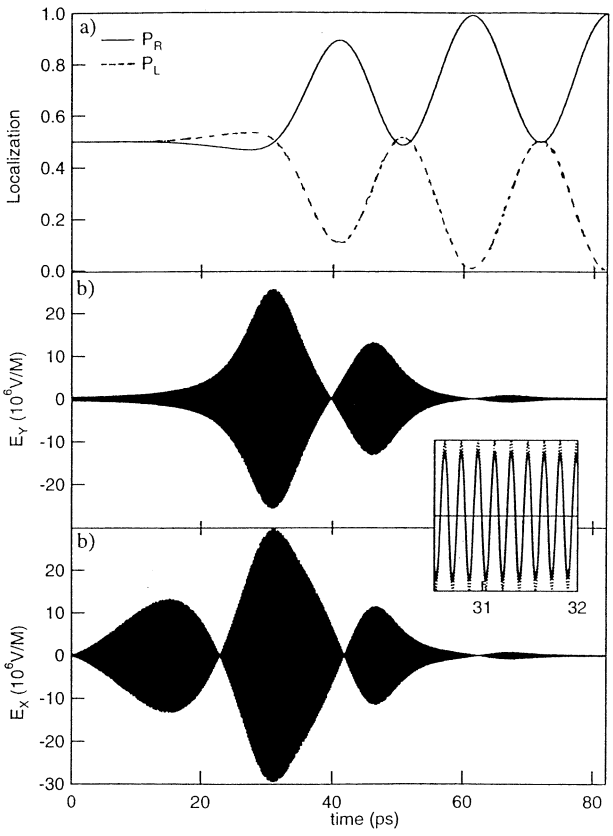

Fig. 15. (a) Population changes in enantiomers localized on the *R*-well (P_R, solid curve) and *L*-well (P_L, broken curve). (b) Locally designed pulse shapes for controlling the enantiomer selective preparation in a mixed state. The inserted figure shows an expanded view of *x*-polarized (solid) and *y*-polarized electric fields (dotted line). These electric fields are characterized having the same phase. [from Ref. 29]

Figure 15b shows the control pulses calculated for the localization of the enantiomers. The upper (solid) and lower (dotted) curves denote the X- and Y- components of the optimized pulses, respectively. The inserted figure shows an expanded view of both the components between 30.5 and 32.0 ps. From this figure, we can see that the two electric field components consist of a central frequency of $\sim$200 cm^{-1} that corresponds to transition frequencies between $|0\pm\rangle$ and $|1\pm\rangle$. We can also see from Fig. 15b that the two electric fields have the same phase, and that the synthesized field from these fields is a linearly polarized one, and is oriented about 60° with respect to the YZ plane as shown in Fig. 16. It should be noted that this orientation of the electric fields is almost parallel to the configuration of the *R*-form of H_2POSH in its equilibrium configuration. We can see from this figure that, by applying a linearly polarized pulse, enantiomers of *L*-form are transferred into those of *R*-form, while the reverse process is suppressed.

2.5 Ring-Puckering Isomerization. As an example of an application of the locally optimized control method based on the control theory of a linearly time-invariant (LTI) system, we deal with a laser-induced ring-puckering isomerization of trimethylenimine.[18] This molecule has two isomers corresponding to the different conformations (isomers A and B) shown in Fig. 17. We restrict ourselves to a one-dimensional model in which the coordinate of the puckering motion q is defined as the displacement of the line joining the carbon and nitrogen atoms.[86] The adiabatic potential curve is also shown in Fig. 17, together with the eigenfunctions. The horizontal lines on which the eigenfunction are drawn denote the eigenvalues. Isomer A, which corresponds to eigenstate $|0\rangle$ localized in the left well, is more stable by 100 cm^{-1} than isomer B, that is, the eigenstate $|1\rangle$, and the energy barrier between those isomers is about 450 cm^{-1}. The dipole moment function is approximated by $\mu(q) = \mu_0 + \mu_1 q$, where $\mu_0 = 0.716$ Å·e and $\mu_1 = 0.310$ e.[87]

Since our main goal is to promote isomerization corresponding to the transition $|0\rangle \rightarrow |1\rangle$, the initial state of the

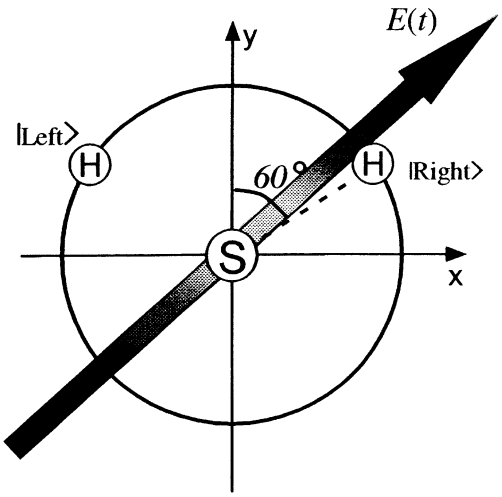

Fig. 16. Optimal electric field polarization synthesized by the two electric fields shown in Fig. 15. Two enantiomer configurations of the *R*- and *L*-forms are also shown. [from Ref. 29]

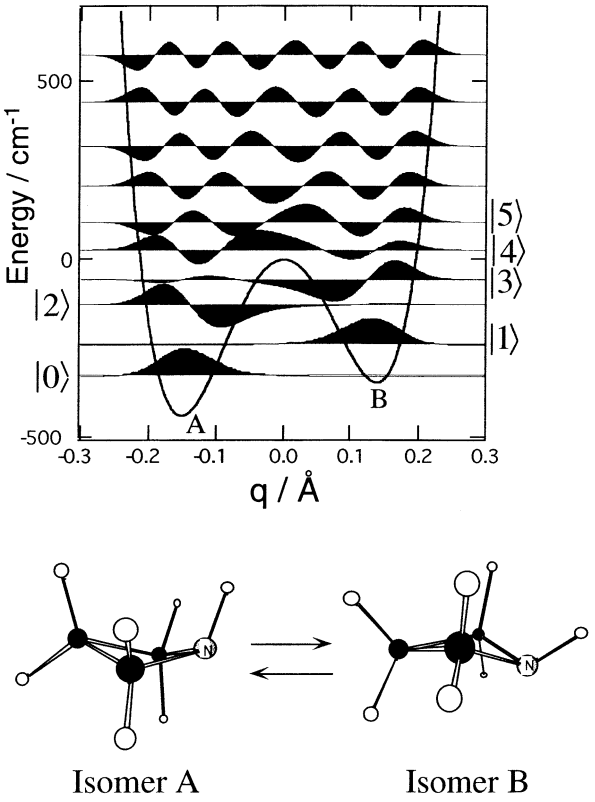

Fig. 17. Adiabatic potential surface of trimethylenimine with respect to the puckering coordinate q and vibrational eigenfunctions $\{\phi_i(q)\}$ (i = 0, 1, ..., 9). [from Ref. 18]

molecule is taken to be the vibrational ground state $|0\rangle$. The transition moment between $|0\rangle$ and $|1\rangle$ is extremely small, since there exists little overlap between these eigenfunctions. Therefore, it is difficult to control the isomerization effectively through the direct transition $|0\rangle \rightarrow |1\rangle$. Here, we take into account several eigenstates other than the initial and final states so that the system can utilize the optically "easy-to-access" eigenstates as intermediate states. Since eigenstate $|4\rangle$ is the lowest delocalized state, we choose five molecular eigenstates (from $|0\rangle$ to $|4\rangle$) for describing the system dynamics. As for choosing control laser fields, we considered two cases: one laser field and four laser fields. The calculations of the isomerization control gave almost the same result for both two cases. Here, we present a four-color laser case.

Under the transition path $|0\rangle \rightarrow ...|m_1\rangle \rightarrow |m_2\rangle... \rightarrow |1\rangle$, the electric field is optimized so that the population of the intermediate state $|m_1\rangle$ becomes smaller than that of the subsequent intermediate state $|m_2\rangle$. The most suitable path is assumed to be $|0\rangle \rightarrow |2\rangle \rightarrow |4\rangle \rightarrow |3\rangle \rightarrow |1\rangle$, which consists of the transitions with the most favorable transition moments. To realize this transition, we set peak intensities of lasers with order of TW cm^{-2}.

Figure 18a shows the time evolution of the population of each vibrational state under optimized controlled fields. The controlled fields are shown in Fig. 18b. It can be seen that each laser field is shaped with a Gaussian-like envelope function with a well-determined carrier frequency. Note that those carrier frequencies are not given beforehand but are obtained

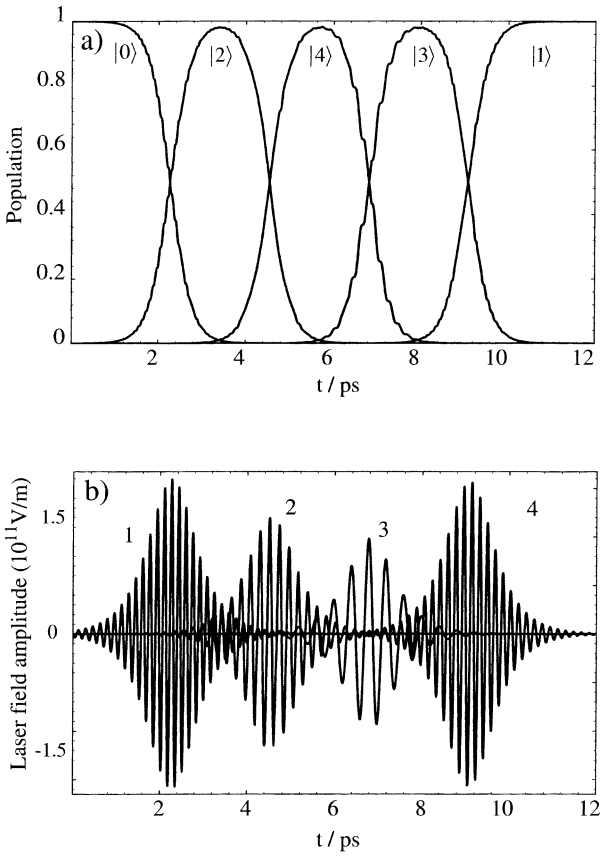

Fig. 18. (a) Time evolution of vibrational eigenstate distribution under the condition of optimized four laser fields as shown in Fig. 18b. [from Ref. 18]

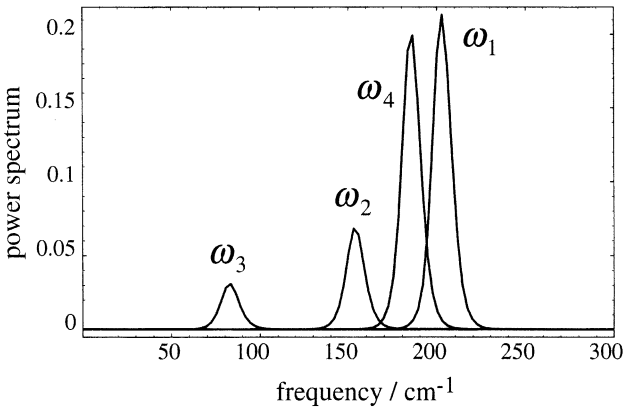

Fig. 19. Power spectrum of the locally optimized laser fields. Each peak indicated by ω_i (i = 1, 2, 3, 4) corresponds to the carrier frequency of the laser fields. [from Ref. 18]

through the local optimization process.

In order to analyze the frequency component of each pulse, we calculated the power spectrum of the optimized field. As shown in Fig. 19, there are four well-separated components. One can see that the central frequency of each peak corresponds to the transition frequency in the preset transition path $|0\rangle \rightarrow |2\rangle \rightarrow |4\rangle \rightarrow |3\rangle \rightarrow |1\rangle$. We calculated the pulse envelope area of each pulse, also defined as

$$\theta_f(t) = \mu_{ij} \int_{t_0}^{t_f} \varepsilon_f^0(t)dt,$$

where $\varepsilon_f(t) = \varepsilon^0_f(t)\sin \omega_f t$, and we obtained $\theta_1 \cong \theta_2 \cong \theta_3 \cong \theta_4 \cong \pi$. This implies that all of the pulses can be regarded as so-called π pulses. Each pulse transfers the population completely as shown in Fig. 18a.

Figure 20 shows the wave packet dynamics expressed as a probability density, $|\langle q|\phi(t)\rangle|^2$, in the optimized laser field. In the early time regime (t = 0–4 ps), the wave packet begins to delocalize. At t = 4–8 ps, the wave packet is delocalized over the two wells because eigenstate $|4\rangle$ is substantially populated at this stage. Finally (at t = 12 ps), the wave packet is almost transferred completely to the well corresponding to isomer B.

For comparison, we show the results obtained in the case of a non-optimized stationary laser field. We preset the four lasers tuned to the transition frequencies comprising the path:

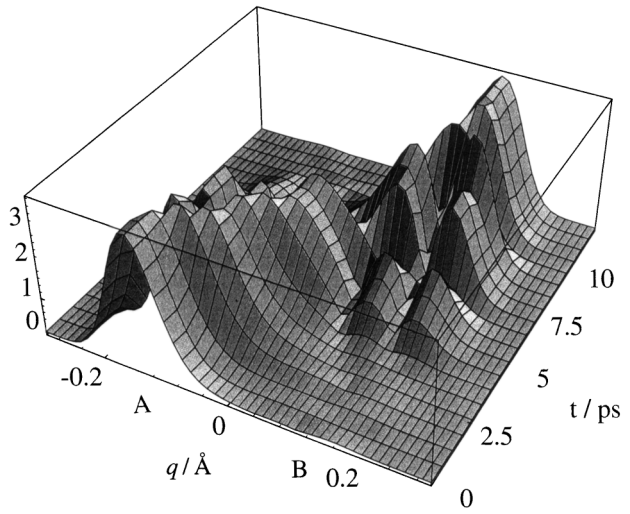

Fig. 20. Wave packet dynamics under the condition of the optimized laser fields, which I is expressed as probability density $|\langle q|\phi(t)\rangle|^2$. [from Ref. 18]

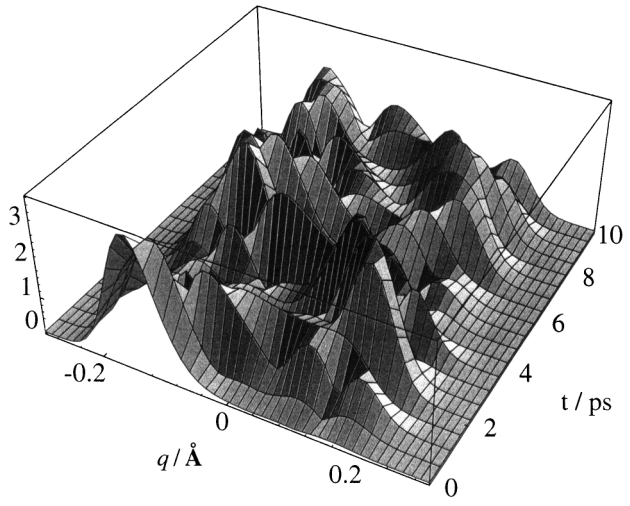

Fig. 21. Wave packet dynamics under the condition of non-optimized stationary laser fields. [from Ref. 18]

$|0\rangle \rightarrow |2\rangle \rightarrow |4\rangle \rightarrow |3\rangle \rightarrow |1\rangle$, i.e., ω_1 = 202.7 cm^{-1}, ω_2 = 153.8 cm^{-1}, ω_3 = 82.8 cm^{-1} and ω_4 = 185.3 cm^{-1}. The intensities I_i corresponding to a laser with the frequency ω_i (i = 1, 2, 3, 4) are taken to be I_1 = 1.0 TW cm^{-2}, I_2 = 0.57 TW cm^{-2}, I_3 = 0.38 TW cm^{-2} and I_4 = 0.97 TW cm^{-2}. Figure 21 shows the wave packet dynamics calculated under the non-optimized stationary field condition. The wave packet remains completely delocalized and there is no localization in the well of isomer B.

2.6 Infrared Multiphoton Dissociation of Hydrogen Fluoride. We now consider quantum control of the photodissociation dynamics of hydrogen fluoride (HF). We obtain the laser field that maximizes the photodissociation yield of HF in the ground electronic state by the locally optimized field. The potential curve and the coordinate dependence of the dipole moment were taken from Ref. 88. This system consists of 23 bound eigenfunctions.

The time-evolution of HF under the optimized laser field condition was obtained by solving the time-dependent Schrödinger equation numerically.[89] The molecular Hamiltonian matrix was obtained through grid discretization of the coordinate space, while time evolution of the wave function was evaluated by operating the short-time propagator expanded in power series. To prevent an undesirable reflection of the wave packet, a portion of the wave packet is eliminated from the propagation when the portion goes beyond the absorbing boundary set in the asymptotic region. The dissociation yield of HF was calculated by collecting the dissociating flux.

Figure 22 shows the population changes in HF as a function of time. In the early time regime (t = 0–8 ps), the population transfers sequentially according to the preset path with the selection rule $\Delta n = n_f - n_i = 1$, where n_i and n_f are vibrational quantum numbers relevant to the transition. This can be readily understood by considering the fact that the lower eigenstates are approximated by those of a harmonic oscillator and $\Delta n = 1$ is the favorable transition among those eigenstates. However, in the following time regime (t = 8–11 ps), the eigenstates $|8\rangle$ and $|10\rangle$ are excluded from the transition path. In the present case, the $\Delta n = 2$ transition $|7\rangle \rightarrow |9\rangle$ is selected by the optimized field, since the transition moment between those states is larger than that between the states $|7\rangle$ and $|8\rangle$. The same sit-

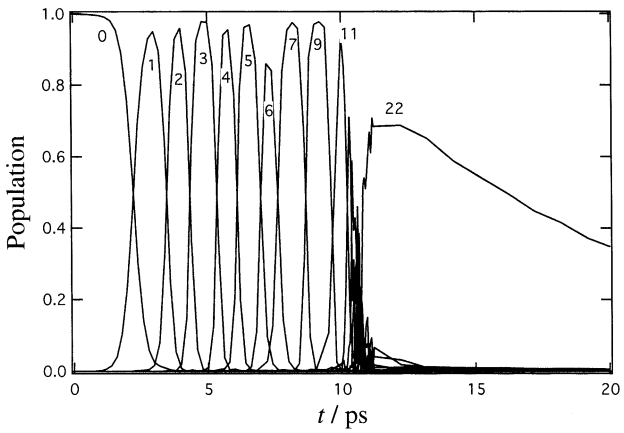

Fig. 22. Time variation of the population of the vibrational eigenstates in the optimized laser field. [from Ref. 89]

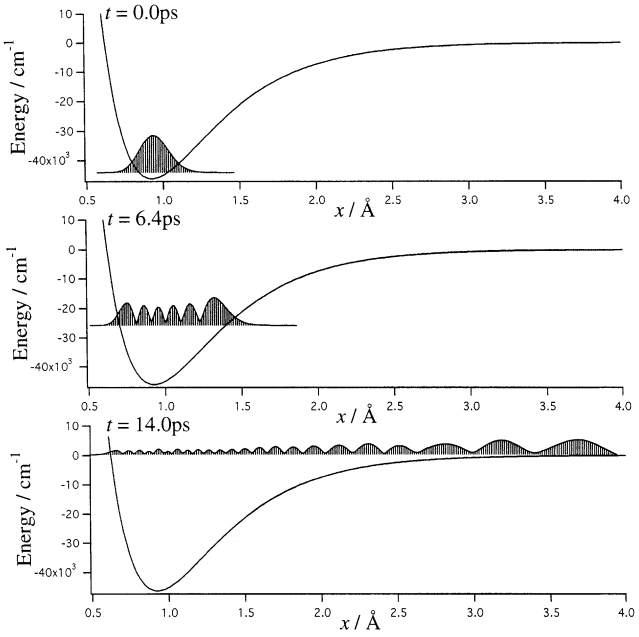

Fig. 23. Wave packet dynamics of HF at the initial time, 6.4 ps and 14.0 ps. The horizontal line refers to the average energy absorbed by HF. [from Ref. 89]

uation can be seen for the $|9\rangle \rightarrow |11\rangle$ transition that skips the eigenstate $|10\rangle$.

Figure 23 shows the wave packet dynamics $|\langle x|\phi(t)|^2$ at the initial time, 6.4 and 14.0 ps under the optimized field condition. The horizontal line on which the wave packet is drawn indicates the average energy of the wave packet. The change in the nodal structure of the wave packet reflects the fact that the wave packet is excited through the sequential transition.

Figure 24a shows the time variation in the optimized laser field. It can be seen that the optimized laser field consists of a sequence of pulses with well-determined carrier frequencies. We extract the modulation of these carrier frequencies from the time-resolved power spectrum shown in Fig. 24b. The time resolution parameter used is taken to be 0.3 ps, which corresponds to the frequency resolution of 111 cm^{-1}. Initially, the carrier frequency is tuned to around 4000 cm^{-1}, which corresponds to the transition frequency of $|0\rangle \leftrightarrow |1\rangle$. In the next time regime (0–8 ps), the carrier frequency is modulated to become smaller and linear with respect to time. This property can be explained by the fact that the level spacing or the $\Delta n = \pm 1$ transition frequency linearly decreases as n increases because of the anharmonicity of the Morse potential curve. This linear frequency modulation seen in the optimized laser field is closely related to the control scheme by chirping pulses.[90–95] The frequency jump from 3000 cm^{-1} to 5200 cm^{-1} that takes place at $t = 8$ ps originates from the fact that the state $|8\rangle$ is excluded from the transition path, as stated above. From $t = 9$ to 12 ps, another linear chirping appears with different carrier frequency components. Since transition moments between higher states are larger than those between lower states, transition processes in this time regime are faster than those occurring during the early time regime ($t = 0$–8 ps). Thus, the chirping rate at $t = 9$–12 ps is higher than that taking place during $t = 0$–8 ps. In the time stage of 9 ps, the dissociation process be-

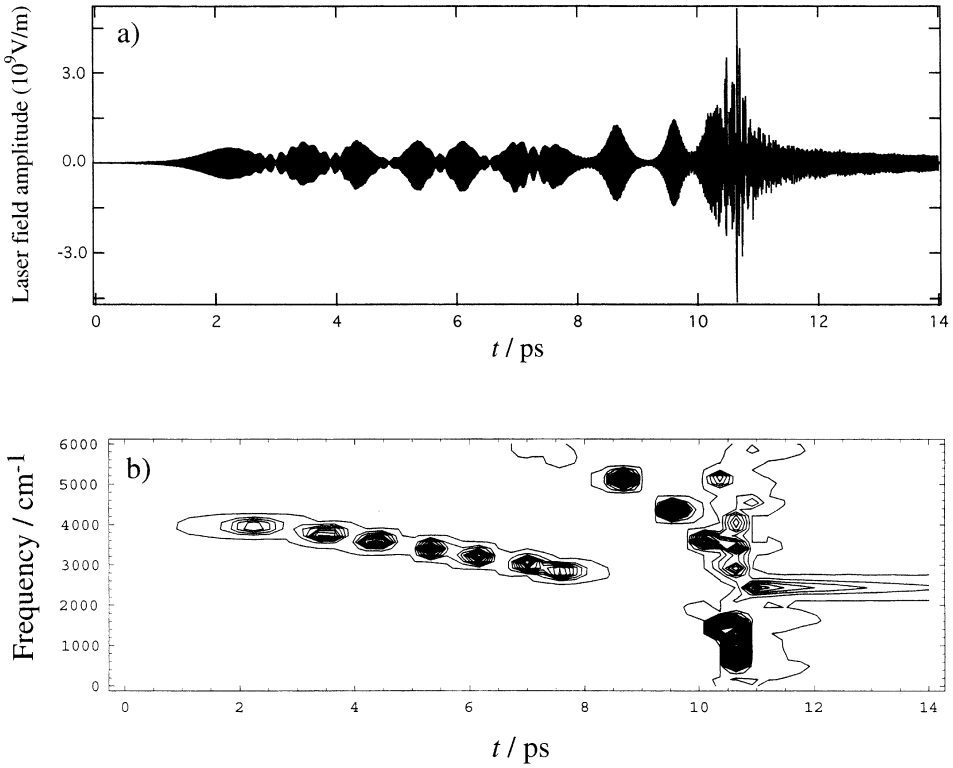

Fig. 24. (a) Time variation of the optimized laser field. (b) Contour map of the time-resolved power spectrum. [from Ref. 89]

gins and many eigenstates are involved in its dynamics, resulting in the complicated structure in the time-resolved power spectrum.

We evaluated the time dependence of the dissociated fraction $Y(t)$. The dissociation yield obtained is about 90%, which demonstrates the effectiveness of the present method. By fitting $Y(t)$ to the exponential function, we can estimate the dissociation rate constant to be 10.2 ps.

For comparison, we also carried out calculation of the wave packet dynamics under the non-optimized, stationary field condition with the same energy fluence as that of the optimized field. Here, we define the energy fluence of the laser field F as

$$F = \int_{t_0}^{t_f} |\varepsilon^0(t)|^2 \, dt.$$

The energy fluence of the present optimized laser field is 5.76 J cm^{-2}. We calculated the population dynamics and the dissociated fraction under the stationary field with the same fluence, which corresponds to the intensity of 0.288 TW cm^{-2}. The frequency of the stationary laser was tuned to the $|0\rangle \leftrightarrow |1\rangle$ transition. The result shows that population transfer occurs only between the two states $|0\rangle$ and $|1\rangle$, and the recurrence feature of the population transfer prevents the molecule from dissociation. On the contrary, the locally optimized laser field produces the dissociation yield of 90%.

2.7 Quantum Control in a Classical Way. Most of the quantum control theories reported so far have been successfully applied to simple reaction systems of one dimension or of a few dimensions, but it is difficult to apply them to the control of reaction dynamics in multidimensional systems. One of the methods for overcoming such a difficulty is to develop a control theory based on classical mechanics, rather than quantum mechanics on which ordinary quantum control theories rely. From the general viewpoint of chemical reaction dynamics, reaction processes can be viewed for a representative point to move from a reactant to a product over a transition state.[96,97] Quantum control of chemical reaction dynamics can be considered in a similar way. That is, a representative point moving on a multidimensional potential surface can be manipulated by a nonstationary laser field. The strategy of this quantum control in a classical way is that the control is carried out by changing the kinetic energy of the representative point of the reaction.[26] The amplitude of the control pulse has a form proportional to the linear momentum of the reaction system. The control field promotes the kinetic motion of the system in the case in which the performance index that represents the deviation from the optimal path becomes smaller and, on the other hand, suppresses the kinetic motion in the case in which performance index becomes larger. In other words, the reaction is controlled by accelerating the representative point on a potential energy surface before it crosses over its potential barrier and then by deaccelerating it to the target after it has passed over the potential barrier.

As an application of this treatment, let us consider isomerization of HCN to HNC in the ground electronic state.[98,99] We use a two-dimensional potential model in which the carbon and nitrogen atom positions are fixed and the hydrogen atom moves on the x–y plane, as shown in Fig. 25. The potential energy surface and the dipole moment function of the reaction

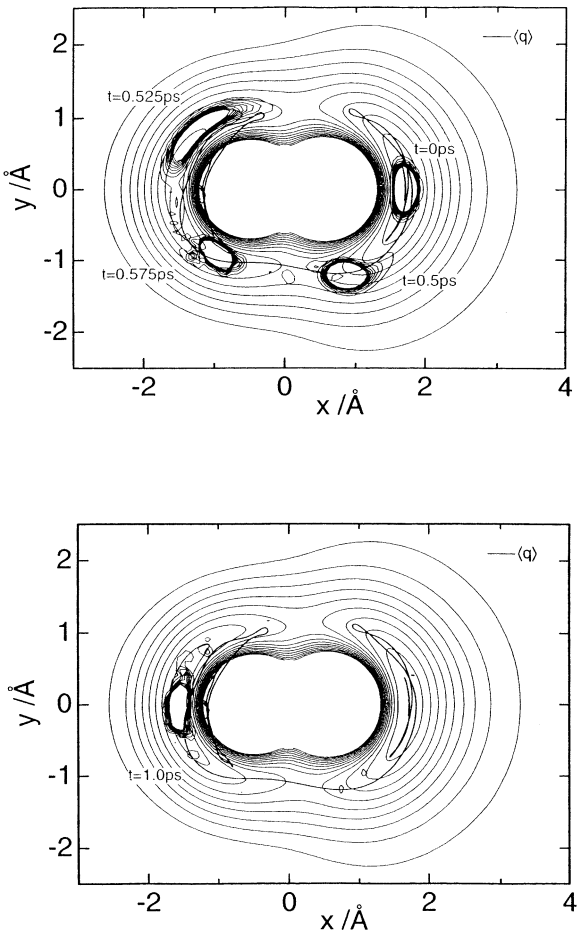

Fig. 25. Snapshots of the wave packet of HCN isomerization (a) in the presence of two linearly polarized control fields, and (b) after. <q> denotes the trajectory of the quantum averaged position of the wave packet. [from Ref. 26]

system were calculated by using the MCSCF method with a 6-311 G(d, p) basis set. Two perpendicular polarized laser pulses are considered to be control fields.[100]

Figure 25 shows snapshots of the wave packets on the potential surface of the ground electronic state. The wave packets are quantum mechanically calculated under the optimized field condition. Each contour with time t denotes the wave packet at that time, and <q> denotes the trajectory of the quantum mechanical average of the position. We can see from this figure that the trajectory runs along the reaction path and that the wave packet moves along the trajectory except for the final course of the reaction. This small difference between the trajectory and the center of each wave packet shows the validity of the classical treatment of quantum control. The wave packet, which is in a vibrationary hot state, overruns the equilibrium point of HNC at 0.525 ps, after crossing the transition state region. Between 0.525 ps and 1 ps, stimulated emission takes place, and the wave packet comes back to the equilibrium point. About 90% of the wave packet is localized in the product region of HNC at the end of the control pulses.

Figure 26 shows the control fields for the isomerization. The upper figure represents the x-polarized field and the lower one represents the y-polarized field. The y-polarized field con-

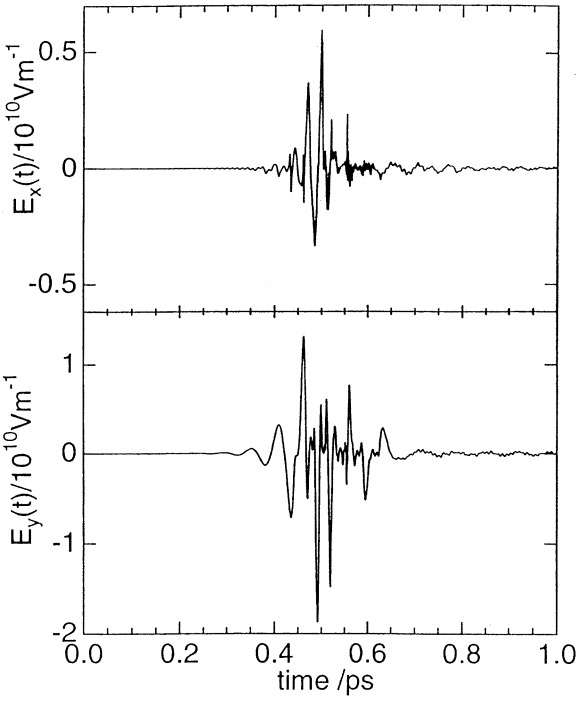

Fig. 26. *x*- and *y*-Polarized fields controlling HCN isomerization. [from Ref. 26]

tributes greatly to controlling the wave packet except for the period in which the system just moves over the reaction barrier. The transition moment of the quantum system implies that the C–H stretching motion is excited faster than C–H bending vibration. However, the wave packet easily moves toward the bending direction because of a low gradient of the potential energy surface to the C–H bending direction, compared with the C–H stretching direction. In the initial stage, the C–H stretching motion is excited by the *x*-polarized pulse, but once the wave packet begins moving in the C–H bending direction, this motion is accelerated by the *y*-polarized pulse. It should be noted that the control pulses generated by the control method described above could not induce another reaction such as dissociation of hydrogen of HCN.

2.8 Quantum Control of Alignment and Orientation. Aligning and orienting molecules along a laboratory fixed plane is essential for stereochemistry and gas-surface chemistry, as well as for selective preparation of enantiomers as described above.[101–103,28] There are several experimental approaches in which uniform external electric fields or intense lasers are utilized to align or orient molecules.[104] Recently, much interest has been paid to alignment and control of molecules using intense laser fields, partly because they can align all molecules with anisotropic polarizability with a much larger degree of alignment than that possible by the other experimental techniques.[105–113] A theoretical method for orientation control of molecules has been proposed by Dion et al.[114] They studied the orientation dynamics of HCN by solving the time-dependent Schrödinger equation, with consideration given to the superpositions of analytical, linearly-polarized infrared laser pulses of frequencies ω and 2ω. We have developed an optimal control theory that is based on global optimization for alignment and orientation of molecules.[30]

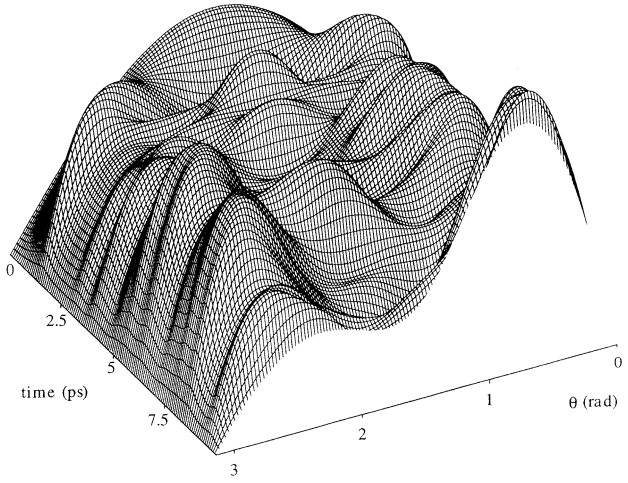

Fig. 27. Time evolution of angular distribution of CO calculated with a target of a a linear combination of spherical harmonics $Y_{0,0}(\vartheta,\phi) + Y_{1,0}(\vartheta,\phi)$ with $\phi = 0$ in the low temperature limit. [from Ref. 30]

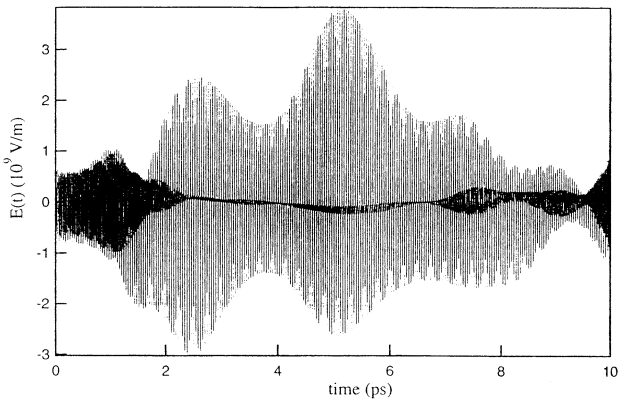

Fig. 28. Optimal laser field for the control of the orientation. [from Ref. 30]

In this subsection, we briefly present the results of orientation control of carbon monoxide (CO), which were obtained by applying the optimal control method. The dipole moment and polarizability of this molecule were taken from Ref. 115. We adopted a linear combination of ϑ-dependent functions of spherical harmonics, $Y_{0,0}(\vartheta,\phi) + Y_{1,0}(\vartheta,\phi)$ with $\phi = 0$, as the target for the orientation of CO. The final time was set to 10 ps.

Figure 27 shows the time evolution of the angular distribution of CO under the optimized laser field condition in the low temperature limit. Here ϑ denotes the latitude in spherical polar coordinates. The peak around $\vartheta = \pi/2$ at the initial time is due to sin ϑ of the element of solid angle. We can see that CO is well oriented at the desired time.

Figure 28 shows the optimized control field for the orientation. To analyze the control field shown in Fig. 28, we evaluated the frequency-resolved power spectrum.

Figure 29 shows a frequency-resolved spectrum in which two sequences of odd and even numbers of $\omega = 850$ cm^{-1} are the main components. The sequence of the odd numbers of ω originates from the polarizability interactions, and that of the

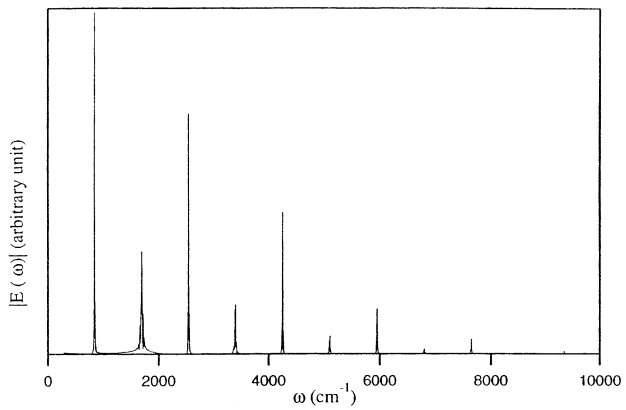

Fig. 29. Frequency-resolved spectrum of the optimal laser field. [from Ref. 30]

even numbers originates from the permanent dipole interaction. The frequency of 1700 cm^{-1} is the fundamental frequency of the CO stretching vibrational mode. It can be seen that the mechanism proposed by Dion et al.[114] and the present mechanism are the same. That is, the simultaneous interactions create rovibrational coherence between the states with odd and even J's, causing symmetry breaking with respect to $\vartheta = \pi/2$. From the classical radiation field theory, the mechanism of the orientation can be explained by differences in the intensity between the plus and minus amplitudes of the pulses, while quantum mechanically the orientation is explained by the interference between 1-photon and 2-photon processes.

3. Towards Attosecond Chemistry

3.1 Intense Field Electronic Dynamics. Application of high-power, ultrashort pulse lasers to molecules results in interesting electronic dynamics such as above-threshold ionization (ATI),[38,39] tunnel ionization,[38–42] and enhanced ionization.[43,44] In the high-intensity and electronically nonresonant low-frequency regime (intensity $I > 10^{13}$ W cm^{-2} and wavelength $\lambda > 700$ nm), the laser electric field significantly distorts the Coulombic potential that the electrons feel. A large part of the electron density is transferred among nuclei within a half optical cycle. Such an intramolecular electronic motion induces nuclear motions. Intense-field-induced nuclear motions can be utilized for control of chemical reactions. It is intriguing to control electron transfer as well as tunnel ionization on an attosecond time scale.

The potential distorted by an intense field forms a "quasi-static" barrier (or barriers) through which an electron or electrons can tunnel. This type of ionization is called tunnel ionization. For the case of atoms, the tunnel ionization regime can be distinguished by using the Keldysh parameter $\gamma = \omega\sqrt{2I_p}/f(t)$,[40] where I_p is the ionization potential of the system, ω is the laser frequency, and $f(t)$ is the pulse envelope at time t. The Keldysh parameter is the ratio of the time required for electron-tunneling through the quasi-static barrier to the optical period $1/\omega$. As the electric field is stronger and its period is longer, an electron penetrates or goes beyond the barrier(s) more easily before the phase of the electric field changes. The quasi-static tunneling condition is given by the inequality $\gamma < 1$, while the ordinary multiphoton ionization (MPI) regime is defined as $\gamma > 1$. The straightforward application of the Keldysh parameter to diatomic and polyatomic molecules is questionable because a zero range (δ-function like) potential is employed in Keldysh's treatment. Recently, DeWitt and Levise has proposed a "modified" Keldysh parameter that takes into account extensive electron delocalization in molecules.[116,117]

In the tunneling regime for molecules, a novel correlation between dissociation and tunnel ionization, known as enhanced ionization, has been discovered;[38,43,44,118,119] the kinetic energies of fragments of a molecule are large ($\gg$ a few eV) and are consistent with Coulomb explosions of multiply charged cations at a *specific internuclear distance* R_c in the range of $\sim 2R_e$,[42] where R_e is the equilibrium internuclear distance. To quantitatively understand such electronic dynamics and combined process with photodissociation, it is necessary to solve the time-dependent Schrödinger equation for electronic degrees of freedom (interacting with the field). We have been developing an efficient grid method, the dual transformation method,[35–37] for accurate propagation of an electronic wave packet. In this method, both the wave function and the Hamiltonian are transformed consistently to overcome the numerical difficulties arising from the divergence of the Coulomb potentials. We have applied this method to small molecular systems such as H_2^+ [120–122] and H_2.[37] The vibrational degree of freedom is also incorporated in the calculation of H_2^+ without resorting to the Born–Oppenheimer approximation.[120–122]

Laser-induced intramolecular electronic motion which triggers tunnel ionization can be analyzed by means of time-dependent "field-following" adiabatic states $\{|n\rangle\}$ defined as eigenfunctions of the "instantaneous" electronic Hamiltonian $H_0(t)$ including the interaction with light.[120–122] To obtain $\{|n\rangle\}$, we diagonalize $H_0(t)$ by using bound eigenstates of the Born–Oppenheimer electronic Hamiltonian H_{el} at zero field as a basis set. Tunnel ionization occurs from such an adiabtic state (or from adiabatic states) to Volkov states[123] (quantum states of a free electron in a laser field). Intramolecular electronic motion also affects nuclear motion; e.g., after one-electron ionization from H_2, the bond distance of the resultant H_2^+ stretches on the lowest adiabatic potential surface.[124–126] In the high-intensity regime, field-following adiabatic potential surfaces can in general cross each other. Field-induced nonadiabatic transitions through avoided crossing points in time and internuclear coordinate space, as well as nuclear motion-induced ones, govern the electronic and nuclear dynamics in intense fields.[120–122,127,128] As mentioned below, laser-induced nuclear motion, as well as the dynamics of bound electrons and the subsequent ionization process, can be understood by analyzing the time-dependent populations of adiabatic states.

The electronic dynamics of H_2^+ prior to tunnel ionization is determined by the radiative dipole coupling $z\varepsilon(t)$ between the highest occupied molecular orbital (MO) and the lowest unoccupied MO, $1s\sigma_g$ and $2p\sigma_u$, respectively.[120–122] Here, z is the electronic coordinate parallel to the molecular axis, and $\varepsilon(t)$ is the axis component of the linearly polarized laser electric field. The dipole transition moment between them, parallel to the molecular axis, increases as $R/2$, where R is the internuclear distance. This large transition moment is characteristic of a charge resonance transition between a bonding and a corre-

sponding antibonding molecular orbital, which was originally pointed out by Mulliken.[129] The strong radiative coupling of the charge resonance transition changes the potential surfaces of $1s\sigma_g$ and $2p\sigma_u$ to "field-following" time-dependent adiabatic surfaces, $E_{\mp}(R)$. The eigenvalues $E_{\mp}(R)$ and corresponding eigenstates $|-\rangle$ and $|+\rangle$ of the instantaneous Hamiltonian $H_0(t)$ are obtained by using two eigenstates, $1s\sigma_g$ and $2p\sigma_u$, of H_2^+:[120–122,130]

$$E_{\mp}(R) \approx \left[E_g + E_u \mp \sqrt{(E_u - E_g)^2 + R^2\varepsilon^2(t)}\right]/2, \quad (22)$$

where E_g and E_u are the eigenvalues of $1s\sigma_g$ and $2p\sigma_u$, respectively. The adiabatic energies $E_{\mp}(R)$ at $\varepsilon(t) = 0.045$ a.u. are shown in Fig. 30 as well as E_g and E_u. The field strength ε in atomic units corresponds to the intensity I as $I = 3.5 \times 10^{16}\ \varepsilon^2$ W cm^{-2}.

The instantaneous electrostatic potential for the electron placed on the molecular axis is plotted for $\varepsilon(t) = 0.07$ a.u in Fig. 31. Here, R is fixed at 4 a.u. The instantaneous potential has two wells around the nuclei, i.e., $z = \pm R/2$. The dipole interaction energy for an electron is $\varepsilon(t)R/2$ at the right nucleus and $-\varepsilon(t)R/2$ at the left nucleus. As $\varepsilon(t)$ increases from zero, the potential well formed around the right nucleus ascends and the well formed around the left nucleus descends.[120–122] Therefore, the ascending and descending wells yield the adiabatic energies E_+ and E_-, respectively, as shown in Fig. 31 ($|+\rangle$ and $|-\rangle$ are localized near the ascending and descending wells, respectively.). Figure 31 also shows that there exist barriers between the two wells (inner barrier) and outside the descending well (outer barrier). As shown in Fig. 30, while E_- is usually below the barrier heights, E_+ can be higher than the barrier heights in the range $R_c = 7$–8 a.u.[131] In this critical range of R, the upper adiabatic state $|+\rangle$ is easier to ionize than is $|-\rangle$. The range of R_c values is consistent with the numerical simulations of ionization.[132,133]

After one-electron ionization from H_2, the bond distance of the resultant H_2^+ stretches on the E_- laser-induced dissociative potential (bond softening due to a laser field)[124–126] and then ionization proceeds via the $|+\rangle$ state that is nonadiabatically created around R_c from $|-\rangle$ when the field $\varepsilon(t)$ changes its sign, i.e., when the two adiabatic potential surfaces come closest to each other. This mechanism of enhanced ionization has been directly proved by monitoring the populations of adiabatic states such as $|+\rangle$ and $|-\rangle$.[120–122] As the field strength approaches a local maximum, a reduction in the population of $|+\rangle$ is clearly observed, whereas the population of $|-\rangle$ changes very little. A nonadiabatic transition between $|+\rangle$ and $|-\rangle$ corresponds to the spatial localization of the electron near a nucleus. Enhanced ionization in H_2^+ is due to electron localization, i.e., suppression of electron transfer between the nuclei (called charge resonance-enhanced ionization[131,132]). The nonadiabatic transition probability can be increased by increasing the intensity, frequency, and R. The above analysis using the populations of two adiabatic states, $|+\rangle$ and $|-\rangle$, is validated by the fact that only two states, $|-\rangle$ and $|+\rangle$, are mainly populated before ionization. Nonadiabatic transitions occur only between the two adiabatic states arising from a charge resonance pair such as $1s\sigma_g$ and $2p\sigma_u$.

3.2 Electronic Wave Packet Dynamics of Multi-Electron Systems. We have succeeded in accurately propagating the two-electron wave packet of H_2 for the first time.[37] In this subsection, we present the results of investigation of the electronic dynamics. The position of the jth electron can be designated

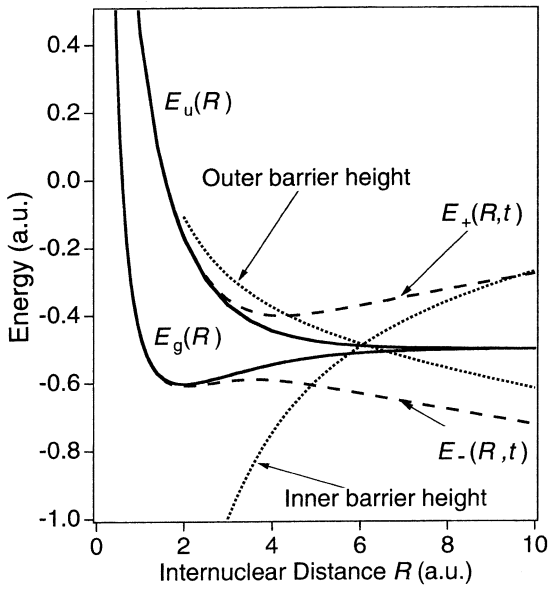

Fig. 30. The lowest two adiabatic potential energies E_- and E_+ (broken lines) of H_2^+ and the heights of the inner and outer barriers (dotted lines) at the field strength $\varepsilon(t) = 0.045$ a.u. as functions of R. The solid lines denote the Born–Oppenheimer surfaces of the lowest two electronic states $1s\sigma_g$ and $2p\sigma_u$.

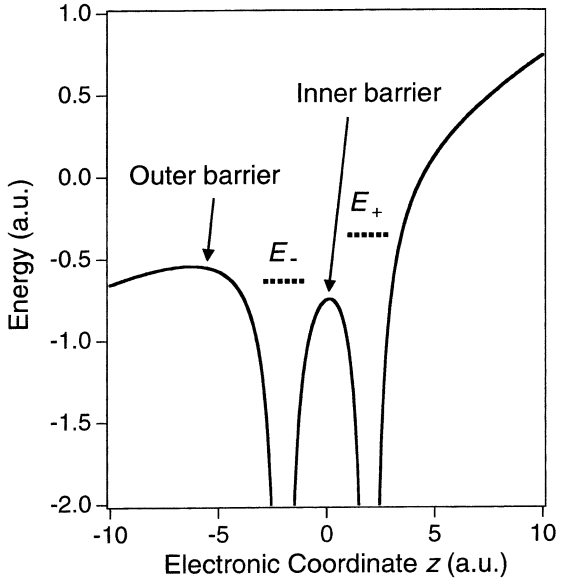

Fig. 31. The H_2^+ instantaneous potential at $\varepsilon(t) = 0.07$ a.u. as a function of the electronic coordinate z along the molecular axis ($R = 4$ a.u.). The polarization direction is assumed to be parallel to the molecular axis. The instantaneous potential has an inner and an outer barrier. The energies of the lowest two "field-following" adiabatic states, E_- and E_+, are denoted by horizontal dotted lines.

by cylindrical coordinates (ρ_j, z_j and φ_j). The z axis is parallel to the molecular axis. Here, we assume that the molecular axis is parallel to the applied field $\varepsilon(t)$ and that the internuclear distance is fixed. We choose the exact ground state at $R = 4$ a.u as an initial state at $t = 0$. The field $\varepsilon(t)$ is assumed to be $f(t)\sin(\omega t)$, where the pulse envelope $f(t)$ is linearly ramped with time t so that after one cycle $f(t)$ attains its maximum ε_0. The field parameters used are $\varepsilon_0 = 0.12$ a.u. and $\omega = 0.06$ a.u. ($\lambda = 760$ nm). The length of a quarter cycle is $\pi/2\omega = 26.2$ a.u.$= 0.634$ fs. The instantaneous field strength is $\varepsilon_{(t)} = 0.03$ a.u. at $t = \pi/2\omega$ and $\varepsilon_{(t)} = -0.09$ a.u. at $t = 3\pi/2\omega$.

Electron transfer in H_2 is characterized by motion along the polarization direction z. Figure 32 shows snapshots of the reduced density $\overline{P}(z_1,z_2)$ obtained by integrating the square of the wave function, $|\psi(t)|^2$, over the degrees of freedom other than z, and Z_2. As shown in Fig. 32a, the covalent components (H·H) around $z_1 = -z_2 = \pm R/2$ are dominant at $t = 0$. The ionic component around the left nucleus, where $z_1 = z_2 = -R/2$, increases as the field approaches the first local maximum at $t = \pi/2\omega$, as shown in Fig. 32b. The laser field forces the two electrons to stay near a nucleus for a half cycle. A quarter cycle later, the field returns to zero. The packet at $t = \pi/\omega$ in Fig. 32c is nearly identical with the initial one in Fig. 32a, indicating that the response to the field is still adiabatic.[134,135] In Fig. 32d, the density around $z_1 = z_2 = R/2$ becomes very high because of the stronger field strength at $t = 3\pi/2\omega$.

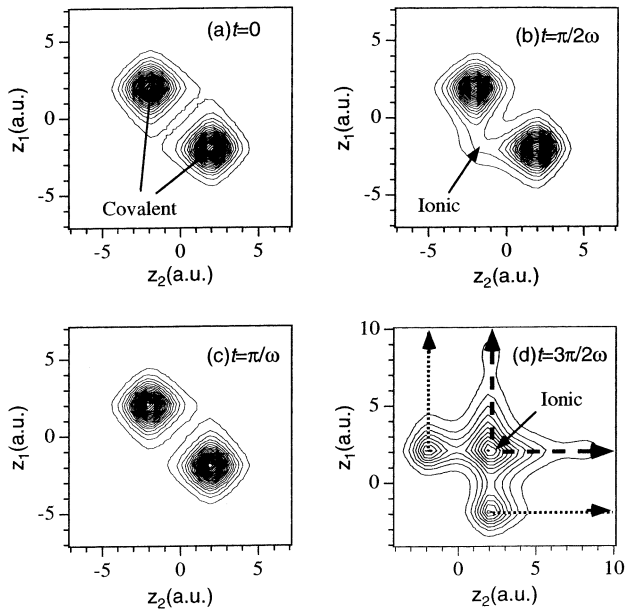

Fig. 32. Snapshots of the electronic wave packet dynamics of H_2 in an intense field. The coordinates z_1 and z_2 for the two electrons are parallel to the molecular axis. The molecule is assumed to be aligned along the field $\varepsilon(t)$. The reduced density $\overline{P}(z_1,z_2)$ obtained by integrating the square of the wave function, $|\psi(t)|^2$, over the other degrees of freedom is drawn at quarter cycle intervals ($\omega = 0.06$ a.u.). The contour intervals are the same for the four panels. The instantaneous field strength is $\varepsilon(t) = 0.03$ a.u. at $t = \pi/2\omega$ and $\varepsilon(t) = -0.09$ a.u. at $t = 3\pi/2\omega$. An ionic component characterized by the structure H^-H^+ or H^+H^- is created near the descending well (where $z\varepsilon(t) < 0$). In (d), the density around the ionic configuration $z_1 = z_2 = R/2$ becomes very high because of the stronger field strength at $t = 3\pi/2\omega$. As indicated by the broken line in (d), an electron is ejected from the localized ionic structure. [from Ref. 37]

From analysis of the spatial configurations of the two electrons, the localized ionic structure is identified with the bound state H^- at the nucleus in the descending potential well. We define the localized ionic structure $|H^+H^-\rangle$ and $|H^-H^+\rangle$ as H^- ions located at $z = \pm R/2$, respectively. At $t = 0$, $|\langle\psi|H^+H^-\rangle|^2 = |\langle\psi|H^-H^+\rangle|^2 = 0.19$. The ionic character increases as the field strength increases; at $t = 3\pi/2\omega$, the ionic character is as large as $|\langle\psi|H^+H^-\rangle|^2 = 0.54$. As indicated by the broken line in Fig. 32d, an electron is ejected from the localized ionic structure. The ionic structure has an ionization potential as low as $I_p(H^-) = 0.75$ eV and is hence regarded as a doorway state to ionization. The direct ionization route from the covalent structure H·H is denoted by a dotted line in Fig. 32d, but the ionization current along the dotted line is relatively small.

At $R = 4$ a.u., the rate of ionization from a *pure* ionic state is greater than that from a *pure* covalent state. As R increases, the rate of ionization from the former state increases owing to the less attractive force of the distant nucleus, while the rate of the latter state is nearly independent of R. On the other hand, the population of the H^-H^+ created decreases with increasing R. As a result, the rate has a peak at the critical distance $R_c =$ 4–6 a.u.[134,135] The mechanism of the creation of the localized ionic state can be analyzed in terms of adiabatic states. The covalent-character-dominated initial state H·H is adiabatically connected with the lowering ionic state H^-H^+ when these two states cross each other.[134,135] If $|\varepsilon(t)|$ goes beyond the intensity required for the crossing, the population of H^- dramatically increases, as shown in Fig. 32d. At large $R > 8$ a.u., the gap at the crossing between the two adiabatic states is very small, i.e., the case is diabatic: the main character is always covalent.

As R decreases, the gap at the avoided crossing between the covalent and ionic states increases, which results in efficient one-electron transfer from the ascending well to the descending well. More efficient electron transfer indicates stronger attraction by the distant nucleus which decreases the ionization rate from a pure H^-H^+. In fact, what correlates with R_c is not just the avoided crossing between the covalent and ionic states but extensive avoided crossing where most adiabatic states avoid each other with considerable gaps.[134] Extensive avoided crossing is observed around $R = 6$ a.u. Avoided crossing with a considerable gap occurs whenever two states that have an ionic character cross.[134] Note that the transition moments due to charge transfer are very large (proportional to R).[129]

It should be pointed out that enhanced ionization or extensively avoided crossing is correlated with efficient Intramolecular Electronic energy Redistribution (IER) around R_c. It is possible to calculate the time-averaged probability $P(i|i)$ of finding the system in a main doorway state to ionization, namely H^-H^+, provided that the initial state is H^-H^+ and the applied field is turned off. Since $P(i|i)$ can be interpreted to be inversely proportional to the phase space volume explored by the dynamics under consideration, the number of background states effectively coupled with H^-H^+, N_{eff}, can be defined as $N_{\text{eff}} + 1 = 1/P(i|i)$.[136,137] Amazingly, the calculated number

N_{eff} has a peak around R_c. As N_{eff} increases, the number of degeneracies lifted increases. IER around R_c is responsible for the extensive avoided crossing and hence correlates with the enhanced ionization.[138]

Nuclear dynamics initiated by laser-induced multi-electron dynamics in polyatomic molecules can be also treated. Ultrafast deformation of molecular structure, which is one such nuclear dynamics, was experimentally investigated for various triatomic molecules such as H_2O,[43] NO_2 [44] and CO_2.[118] At present, it is virtually impossible to accurately solve the time-dependent Schrödinger equation for such multi-electron molecules. However, characteristic features of electronic dynamics in intense laser fields such as electron localization in H_2^+ [120–122] and electron transfer in H_2,[37,134,135] brings us a simple electrostatic model where each atom of a molecule is characterized by its charge.[139,140] For H_2, tunnel ionization is governed by the population of unstable localized ionic components H^-H^+ and H^+H^- and by the distance between the positive and negative charges. We thus propose the idea that each atom in a molecule is charged by electron transfer in intense laser fields and ionization proceeds via the most unstable atomic site, i.e., the most negatively (or least positively) charged site. The ionization rate of a localized ionic component created increases as the distance between the opposite charges increases.

The above idea allows us to use a practical theoretical approach for multi-electron molecules, i.e., ab initio MO methods. While the adiabatic potential surfaces calculated predict whether or not the molecule is deformed, the charge distributions can be used to estimate the probability of tunnel ionization. This approach is simple but it has wide applicability in predicting the *electronic* and *nuclear* dynamics of large molecules in intense laser fields. We have revealed the mechanism of the experimentally observed large amplitude bending motion of CO_2.[141]

3.3 Attosecond Dynamics. In the high-intensity and low-frequency regime, the electronic wave function changes drastically within a half optical cycle, i.e., on an attosecond scale. Laser control in this regime will therefore bring about ultrafast (intermolecular and intramolecular) electron transfer on a massive scale. The initiated electronic motion also brings about bond formation and bond cleavage. The target will extend from small molecules toward large polyatomic molecules and extended structure systems (clusters, aggregates, polymers, and solid state materials).

The charge distribution in a molecule can be changed by an intense field. For butadiene, in a relatively weak field, the four carbon atoms are charged alternately with positive and negative charges. When the field intensity approaches 10^{14} W cm^{-2}, only the two end-carbon atoms are charged so that a large induced dipole moment is created. The change in charge distribution induces a different mechanism of tunnel ionization (The atomic site that ionization proceeds from varies.), which changes fragment species due to resultant Coulomb explosions. It may be possible to break a specific bond by controlling Coulomb explosions. It is also interesting to utilize the difference in bond softening in an intense field between isotopes. Bond-selective cleavage of an HOD molecule can be designed (The speed of bond softening of the O–H bond is expected to be faster than that of the O–D bond.).

As observed in H_2, an electron pair is formed in an intense field. If the field could be suddenly turned off, an electron pair would be prepared. Although the populations of H^-H^+, H^+H^- and H·H change, the electron pair can survive (though radiative damping due to higher-order harmonic generation[142–144] take place). Nonadiabatic switching-off of a field can prepare many ionic sites in a polyatomic molecule. The questions to be answered are as follows: How many ionic sites are created?; How does delocalization of the charge density occur?; Do soliton waves exist in the subsequent charge migration?[145] Super ultrafast control of this kind of electronic dynamics by shaping attosecond pulses would have a great impact on the evolution of science and technology in the new century.[146] We are currently developing a theoretical approach to quantum control of electronic dynamics of molecules.

4. Summary

In this paper, we presented a theoretical treatment of quantum control of reaction dynamics. We first described the development of effective methods for designing locally optimized laser fields to control wave packets. Locally designed optimal control methods have been applied to simple unimolecular reactions such as isomerization of trimethylenimine and predissociation of NaI. These systems are controlled by methods such as pump–probe type, multiple sequential transitions and chirping control, depending on both the vibrational structures and dipole moment functions of the reaction system. Quantum control of selective preparation of H_2POSH with dynamic chirality was treated on the basis of density matrix formulation. The most important parameter of optimal control pulses in the selective preparation from its L-form to *R*-form is polarization of two laser fields. The synthesized field of the two electric fields is a linearly polarized field that is almost parallel to the *S*-H bond of the *R*-form of H_2POSH in its equilibrium configuration. The control mechanism is as follows. By applying the linearly polarized pulse to the racemic mixture, enantiomers of L-form are transferred into those of *R*-form, while its reverse process is suppressed. The control theory was also applied to the population manipulation of dark states of a molecule and to alignment and orientation control. It should be noted that the local control theory is applicable to weak field cases as well as to strong field cases.

We next introduced an accurate grid point method for solving the time-dependent Schrödinger equation for the electronic degrees of freedom of a system, namely, the dual transformation method. Accurate propagation of an electronic wave packet is essential for understanding and controlling intramolecular electron transfer dynamics in intense laser fields and for controlling chemical reactions through intramolecular electron transfer. We have applied the dual transformation method to H_2^+ and H_2 in intense fields ($I > 10^{13}$ W cm^{-2}). To comprehend the ultrafast dynamics of intramolecular electron transfer, field-induced structure deformation, and subsequent tunnel ionization processes, we map the electronic wave packet onto "field-following" adiabatic states defined as eigenfunctions of the "instantaneous" electronic Hamiltonian. The mechanisms of the intense-field-induced phenomena mentioned above have been clarified by monitoring the populations of adiabatic states. For H_2, the localized ionic state created in an intense

field works as the main doorway state to tunnel ionization. The deformation or dissociation of a molecule in intense laser fields, such as that observed in H_2^+, can be understood as the nuclear dynamics on the time-dependent potential surfaces of adiabatic states. These results lead to the simple idea that each atom of a molecule in an intense field is charged by electron transfer and the charge distribution determines the adiabatic potential surface on which the nuclear wave packet propagates. On the basis of this idea, we have proposed possible control scenarios such as bond-selective cleavage of an HOD molecule.

A combined treatment of the propagation of the electronic wave packets with optimal control theory will create new scenarios for the attosecond control of electronic and subsequent nuclear motions by intense laser fields. The ultimate combination provides a theoretical foundation for attosecond chemistry as well as for the developments of attosecond laser technology.

We would like to thank Professor J. Manz and Professor A. D. Bandrauk for their stimulating discussions and fruitful comments. We gratefully acknowledge many collaborators, Professor S. Koseki, Professor T. Kobayashi, Professor S. Sato, Professor M. Hayashi, Dr. H. Umeda, Dr. Y. Nomura, Dr. T. Kato, Dr. K. Amano, Dr. I. Kawata, Dr. L. González, Dr. S. Chelkowsky, Mr. K. Hoki, Mr. A. Kita, Mr. T. Watanabe, Mr. Nakagami, Mr. T. Taneichi, Mr. K. Harumiya, Mr. D. Kröner, Mr. G. Sugiyama, Ms. Y. Kurosawa, Ms. M. Kato, Mr. Y. Yahata, Mr. T. Sato, and Mr. T. Noguchi. This work was partly supported by a German–Japan International Joint research project, by Grants-in-Aid for Scientific Research (No. 10640480, 10044054 and 12640484), by a Grant-in-Aid for Scientific Research on Priority Areas (No. 11166205) and by the Development of High-Density Optical Pulse Generation and Advanced Material Control Techniques.

References

1 P. Brumer and M. Shapiro, *Annu. Rev. Phys. Chem.*, **43**, 257 (1992); M. Shapiro and P. Brumer, Adv. In Atom. Mol. And Opt. Phys., 42, Academic, Sandiego (1999) p. 287.

2 B. Kohler, J. L. Krause, F. Raksi, K. R. Wilson, V. V. Yakovlev, R. M. Whitnell, and Y. J. Yan, *Acc. Chem. Res.*, **28**, 133 (1995).

3 A. Assion, T. Baumert, M. Bergt, T. Brixner, B. Kiefer, V. Seyfried, M. Strehle, and G. Gerber, *Science*, **282**, 919 (1998).

4 R. J. Gordon, L. Zhu, and T. Seideman, *Chem. Res.*, **32**, 1007 (1999).

5 D. Goswami and A. S. Sandhu,. *Adv. Multi-photon Processes Spectrosc.*, **13**, 132 (2001).

6 R. Uberna, M. Khalil, R. M. Williams, J. M. Papanikolas, and S. R. Leone, *J. Chem. Phys.*, **108**, 9259 (1998).

7 S. M. Park, S.-P. Lu, and R. J. Gordon, *J. Chem. Phys.*, **94**, 8622 (1991).

8 A. Sugita, M. Mashino, M. Kawasaki, Y. Mathumi, R. J. Gordon, and R. Bersohn, *J. Chem. Phys.*, **112**, 2164 (2000).

9 D. J. Tannor and S. A. Rice, *Adv. Chem. Phys.*, **70**, 441 (1988).

10 S. Shi, A. Woody, and H. Rabitz, *J. Chem. Phys.*, **88**, 6870 (1988).

11 R. Kosloff, S. A. Rice, P. Gaspard, S. Tersigni, and D. J. Tannor, *Chem. Phys.*, **139**, 201 (1989).

12 W. Jakubetz, J. Manz, and H.-J. Schreiber, *Chem. Phys. Lett.*, **165**, 100 (1990).

13 S. Shi and H. Rabitz, *J. Chem. Phys.*, **92**, 364 (1990).

14 P. Gross, D. Neuhauser, and H. Rabitz, *J. Chem. Phys.*, **96**, 2834 (1992); P. Gross, D. Neuhauser, and H. Rabitz, *J. Chem. Phys.*, **98**, 4557 (1993).

15 K. Sundermann and Regina de Vivie-Riedle, *J. Chem. Phys.*, **110**, 1896 (1999).

16 L. Shen and H. Rabitz, *J. Chem. Phys.*, **100**, 4811 (1994).

17 H. Shen, J.-P. Dussault, and A. D. Bandrauk, *Chem. Phys. Lett.*, **221**, 498 (1994).

18 M. Sugawara and Y. Fujimura, *J. Chem. Phys.*, **100**, 5646 (1994).

19 M. Sugawara and Y. Fujimura, *J. Chem. Phys.*, **101**, 6586 (1994).

20 Y. Fujimura, "Structure and Dynamics of Electronic Excited States," Springer-Verlag, Berlin (1999) p. 214.

21 Y. Ohtsuki, K. Nakagami, and Y. Fujimura, *Adv. Multiphoton Processes Spectrosc.*, **13**, 3 (2001).

22 M. Dantus, M. J. Rosker, and A. H. Zewail, *J. Chem. Phys.*, **87**, 2395 (1987).

23 A. Zewail and R. Bernstein, "The Chemical Bond, Structure and dynamics," ed by A. Zewail, Academic press, San Diego (1992), Chap. 9, P. 223.

24 Y. Watanabe, H. Umeda, Y. Ohtsuki, H. Kono, and Y. Fujimura, *Chem. Phys.*, **217**, 317 (1997).

25 Y. Ohtsuki, H. Kono, and Y. Fujimura, *J. Chem. Phys.*, **109**, 9318 (1998).

26 H. Umeda and Y. Fujimura, *J. Chem. Phys.*, **113**, 3510 (2001)

27 K. Hoki, Y. Ohtsuki, H. Kono, Y. Fujimura, and S. Koseki, *Bull. Chem. Soc., Jpn.*, **72**, 2665 (1999).

28 K. Hoki, Y. Ohtsuki, H. Kono, and Y. Fujimura, *J. Phys. Chem. A*, **103**, 6301 (1999).

29 K. Hoki, Y. Ohtsuki, and Y. Fujimura, *J. Chem. Phys.*, **114**, 1575 (2001).

30 K. Hoki and Y. Fujimura, Chem. Phys., **267**, 187 (2001).

31 K. Bergmann, H. Theuer, and B. W. Shore, *Rev. Mod. Phys.*, **70**, 1003 (1998).

32 Y. Ohta, T. Yoshimoto, and K. Nishikawa, *Chem. Phys. Lett.*, **316**, 551 (2000).

33 Y. Teranishi and H. Nakamura, *Phys. Rev. Lett.*, **81**, 2032 (1998).

34 Y. Teranishi and H. Nakamura, *J. Chem. Phys.*, **111**, 1415 (1999).

35 H. Kono, A. Kita, Y. Ohtsuki, and Y. Fujimura, *J. Comput. Phys.*, **130**, 148 (1997).

36 I. Kawata and H. Kono, *J. Chem. Phys.*, **111**, 9498 (1999).

37 K. Harumiya, I. Kawata, H. Kono, and Y. Fujimura, *J. Chem. Phys.*, **113**, 8953 (2000).

38 "Atoms in Intense Fields," ed by M. Gavrila, Academic Press, NewYork (1992).

39 J. H. Eberly, J. Javanainen, and K. Rzazewski, *Phys. Rep.*, **204**, 331 (1991); M. Lewenstein, K. C. Kulander, K. J. Schafer; P. H. Bucksbaum, *Phys. Rev. A*, **51**, 1495 (1995).

40 L. V. Keldysh, *Sov. Phys. JETP*, **20**, 1307 (1965); F. H. M. Faisal, *J. Phys. B*, **6**, L89 (1973); S. Augst, D. D. Meyerhofer; D. Strickland, and S. L. Chin, *J. Opt. Soc. Am. B*, **8**, 858 (1991); M. V. Ammosov, N. B. Delone, and V. P. Krainov, *Sov. Phys., JETP*, **64**, 1191 (1986).

41 V. P. Krainov, H. R. Reiss, and B. M. Smirnov, "Radiative

Processes in Atomic Physics," Wiley, New York (1997).
42 J. H. Posthumus, A. J. Giles, M. R. Thompson, and K. Codling, *J. Phys., B*, **29**, 5811 (1996); K Codling, and L. J. Frasinski, *J. Phys., B*, **26**, 783 (1993).
43 J. H. Sanderson, A. El-Zein, W. A. Bryan, W. R. Newell, A. J. Langley, and P. F. Taday, *Phys. Rev. A*, **59**, R2567 (1999).
44 A. Hishikawa, A. Iwamae, and K. Yamanouchi, *J. Chem. Phys.*, **111**, 8871 (1999).
45 J. Kou, V. Zhakhovskii, S. Sakabe, K. Nishihara, S. Shimizu, S. Kawato, M. Hashida, K. Shimizu, S. Bulanov, Y. Izawa, Y. Kato, and N. Nakashima, *J. Chem. Phys.*, **112**, 5012 (2000).
46 E. Constant, H. Stapelfelt, and P. B. Corkum, *Phys. Rev. Lett.*, **76**, 4140 (1996).
47 M. Schmidt, D. Normand, and C. Cornaggia, *Phys. Rev. A*, **50**, 5037 (1994).
48 S. Chelkovski, P. B. Corkum, and A. D. Bandrauk, *Phys. Rev. Lett.*, **82**, 3416 (1999).
49 J. A. Syage, P. M. Felker, and A. H. Zewail, *J. Chem. Phys.*, **81**, 4706 (1984).
50 R. P. Krawczyk, K. Malsch, G. Hohlneicher, R. C. Gillen, and W. Domcke, *Chem. Phys. Lett.*, **320**, 535 (2000).
51 R. Mathies, C. H. Brito Cruz, W. T. Pollard, C. V. Shank, *Science*, **240**, 778 (1988).
52 Y. Ohtsuki, Y. Yahata, H. Kono, and Y. Fujimura, *Chem. Phys. Lett.*, **287**, 627 (1998).
53 T. Rose, M. Rosker, and A. Zewail, *J. Chem. Phys.*, **88**, 6672 (1988).
54 H. Kono and Y. Fujimura, *Chem. Phys. Lett.*, **184**, 518 (1992).
55 T. Taneichi, T. Kobayashi, Y. Ohtsuki, and Y. Fujimura, *Chem. Phys. Lett.*, **231**, 50 (1994).
56 C. J. Bardeen, J. Che, K. R. Wilson, V. V. Yakovlev, P. Cong, B. Kohler, J. L. Krause, and M. Messina, *J. Phys. Chem. A*, **101**, 3815 (1997).
57 H. Tang and S. A. Rice, *J. Phys. Chem. A*, **101**, 9587 (1997).
58 J. C. Polanyi and A. H. Zewail, *Acc. Chem. Res.*, **28**, 119 (1995), and references therein.
59 J. L. Herek, A. Materny, and A. H. Zewail, *Chem. Phys. Lett.*, **228**, 15 (1994).
60 V. Engel and H. Metiu, *J. Chem. Phys.*, **90**, 6116 (1989).
61 J. L. Krause, R. M. Whitnell, K. R. Wilson, Y. J. Yan, and S. Mukamel, *J. Chem. Phys.*, **99**, 6562 (1993).
62 K. Mishima and K. Yamashita, *J. Chem. Phys.*, **110**, 7756 (1999).
63 K. Misawa and T. Kobayashi, *J. Chem. Phys.*, **110**, 7756 (1999).
64 G. Cerullo, C. J. Bardeen, Q. Wang, and C. V. Shank, *Chem. Phys. Lett.*, **262**, 362 (1996).
65 C. J. Bardeen, Q. Wang, and C. V. Shank, *Phys. Rev. Lett.*, **75**, 3410 (1995).
66 J. Cao, C. J. Bardeen, and K. R. Wilson, *Phys. Rev. Lett.*, **80**, 1406 (1998).
67 J. Cao, J.Che, and K. R. Wilson, *J. Phys. Chem. A*, **102**, 4284 (1998).
68 E. Hiroike and Y. Fujimura, *J. Chem. Phys.*, **86**, 2510 (1987).
69 C. Iung and R. E. Wyatt, *J. Chem. Phys.*, **99**, 2261 (1993).
70 R. Bigwood, B. Milan, and M. Gruebele, *Chem. Phys. Lett.*, **287**, 333 (1998).
71 T. A. Holme, and J. S. Hutchinson, *Chem. Phys. Lett.*, **124**, 181 (1986); T. A. Holme, and J. S. Hutchinson, *J. Chem. Phys.*, **84**, 5455 (1986).
72 Y. Inoue, *Chem. Rev.*, **92**, 741 (1992).
73 M. Avalos, R. Babiano, P. Cintas, J. Jimenez, J. C. Palacios, and L. D. Barron, *Chem. Rev.*, **98**, 2391 (1998).
74 M. Shapiro and P. Brumer, *J. Chem. Phys.*, **95**, 8658 (1991).
75 J. A. Cina and R. A. Harris, *J. Chem. Phys.*, **100**, 2531 (1994); *Science*, **267**, 832 (1995)
76 J. Shao and P. Hänggi, *J. Chem. Phys.*, **107**, 9935 (1997); *Phys. Rev., A*, **56**, R4397 (1997).
77 Y. Fujimura, L. González, K. Hoki, J. Manz, and Y. Ohtsuki, *Chem. Phys. Lett.*, **306**, 1 (1999); *ibid*, **310**, 578 (1999).
78 M. Shapiro, E. Frishman, and P. Brumer, *Phys. Rev. Lett.*, **84**, 1669 (2000).
79 Y. Fujimura, L. González, K. Hoki, D. Kröner, J. Manz, and Y. Ohtsuki, *Angew. Chem.*, **39**, 4586 (2000).
80 O. Kühn, D. Malzahn, and V. May, *Intn. J. Quant. Chem.*, **57**, 343 (1996).
81 M. V. Korolkov, J. Manz, and G. K. Paramonov, *J. Phys. Chem.*, **101**, 13927 (1995).
82 Y. Ohtsuki, W. Zhu, and H. Rabitz, *J. Chem. Phys.*, **110**, 9825 (1999); Y. Ohtsuki, K. Nakagami, Y. Fujimura, W. Zhu and H. Rabitz, *J. Chem. Phys.*, **114**, 8867 (2001).
83 J. M. Yuan, W -K, Liu, M. Hayashi, and S. H. Lin, *J. Chem. Phys.*, **110**, 3828 (1999).
84 A. E. Rowan, and R. J. M. Nolte, *Angew. Chem.*, **37**, 63 (1998).
85 K. Fuji and T. Kawabata, *Chem. Eur. J.*, **4**, 373 (1998).
86 L. A. Carreira and R. C. Lord, *J. Chem. Phys.*, **51**, 2735 (1969).
87 S. C. Leasure, K. F. Milfeld, and R. E. Wyatt, *J. Chem. Phys.*, **74**, 6197 (1981).
88 J. R. Stine and D. W. Noid, *Opt. Commun.*, **31**, 161 (1979).
89 M. Sugawara and Y. Fujimura, *Chem. Phys.*, **196**, 113 (1995).
90 S. Chelkowski, A. D. Bandrauk, P. B. Corkum, *Phys. Rev. Lett.*, **65**, 2355 (1990).
91 S. Chelkowski and A. D. Bandrauk, *Chem. Phys. Lett.*, **186**, 264 (1991).
92 J. E. Combariza, S. Görtler, B. Just, and J. Manz, *Chem. Phys. Lett.*, **195**, 393 (1992).
93 B. Just, J. Manz, and G. K. Paramonov, *Chem. Phys. Lett.*, **193**, 429 (1992).
94 S. Chelkowski and A. D. Bandrauk, *J. Chem. Phys.*, **99**, 4279 (1993).
95 J. Jansky, P. Adam, An. V. Vinogradov, and T. Kobayashi, *Chem. Phys. Lett.*, **213**, 368 (1993).
96 H. Eyring, S. H. Lin, and S. M. Lin, "Basic Chemical Kinetics," Wiley, New York, (1980).
97 "Advances in Classical Trajectory Methods," ed by W. L. Hase, JAI Press, Greenwich, (1992), Vol. 1.
98 C. M. Dion, S. Chelkowski, A. D. Bandrauk, H. Umeda, and Y. Fujimura, *J. Chem. Phys.*, **105**, 9083 (1996).
99 T. Watanabe, H. Umeda, Y. Fujimura, and A. D. Bandrauk, *J. Mol. Struct. Theochem*, **461**, 317 (1999).
100 H. Umeda, M. Sugawara, Y. Fujimura, and S. Koseki, *Chem. Phys. Lett.*, **229**, 233 (1994).
101 R. D. Levine and R. B. Bernstein, "Molecular Reaction Dynamics," Oxford University Press, New York, (1974).
102 Stereodynamics of Chemical Reactions (Special issue), *J. Phys. Chem. A*, **101** (1997).

103 R. Neuhauser, and H. J. Neusser, *J. Chem. Phys.*, **103**, 5362 (1995).
104 L. Hongzhi, J. F. Karen, J. H. Rebecca, and K. Wei, *J. Phys. Chem. A*, **102**, 8084 (1998), and references therein.
105 B. Friedrich, D. P. Pullman, and D. Herschbach, *J. Phys. Chem.*, **95**, 8118 (1995).
106 D. Normand, L. A. Lompre, and C. Cornaggia, *J. Phys. B: At. Mol. Opt. Phys.*, **25**, L497 (1992).
107 B. Friedrich and D. Herschbach, *Phys. Rev. Lett.*, **74**, 4623 (1995).
108 W. Kim and P. M. Felker, *J. Chem. Phys.*, **104**, 1147 (1996).
109 H. Sakai, C. P. Safvan, J. J. Larsen, K. M. Hilligsoe, K. Hald, and H. Stapelfeldt, *J. Chem. Phys.*, **110**, 10235 (1999).
110 J. Larsen, H. Sakai, C. P. Safvan, I. W-Larsen, and H. Stapelfeldt, *J. Chem. Phys.*, **111**, 7774 (1999).
111 J. Ortigoso, M. Rodriguez, M. Gupta, and B. Friedrich, *J. Chem. Phys.*,**110**, 3870 (1999).
112 T. Sideman, *Phys. Rev. Lett.*, **83**, 4971 (1999).
113 A. Keller, C. M. Dion, and O. Atabek, *Phys.Rev. A*, **61**, 23409 (2000).
114 C. M. Dion, A. D. Bandrauk, O. Atabek, A. Keller, H. Umeda, and Y. Fujimura, *Chem. Phys. Lett.*, **302**, 215 (1999).
115 G. Maroulis, *J. Phys. Chem.*, **100**, 13466 (1996).
116 M. J. DeWitt and R. J. Levis, *Phys. Rev. Lett.*, **81**, 5101 (1998).
117 M. J. DeWitt and R. J. Levis, *Phys. Rev. Lett.*, **81**, 5101 (1998).
118 C. Cornaggia, *Phys. Rev. A*, **54**, R2555 (1993); A. Hishikawa, A. Iwamae, and K. Yamanouchi, *Phys. Rev. Let.*, **83**, 1127 (1999).
119 K. W. D. Ledingham, R. P. Singhal, D. J. Smith, T. McCanny, P. Graham, H. S. Kilic, W. X. Peng, S. L. Wang, A. J. Langley, P. F. Taday, and C. Kosmidis, *J. Phys. Chem. A*, **102**, 3002 (1998).
120 I. Kawata, H. Kono, and Y. Fujimura, *J. Chem. Phys.*, **110**, 11152 (1999).
121 I. Kawata, H. Kono, and Y. Fujimura, *Chem. Phys. Lett.*, **289**, 546 (1998).
122 H. Kono and I. Kawata, "Advances in Multi-Photon Processes and Spectroscopy," ed by R. Gordon and Y. Fujimura, World Scientific, Singapore, (2001), Vol. 14, p. 165.
123 M. H. Mittleman, "Introduction to the Theory of Laser-Atom Interactions," 2nd ed, Prenum, New York (1993).
124 A. Zavriyev, P. H. Bucksbaum, J. Squier, and F. Saline, *Phys. Rev. Lett.*, **70**, 1077 (1993).
125 T. D. G. Walsh, F. A. Ilkov, S. L. Chin, F. Châteauneuf, T.-T. Nguyen-Dang, S. Chelkowski, A. D. Bandrauk, and O. Atab ek, *Phys. Rev. A*, **58**, 3922 (1998).
126 T.-T. Nguyen-Dang, F. Châteauneuf, S. Manoli, O. Atabek, and A. Keller, *Phys. Rev. A*, **56**, 2142 (1997).
127 A. D. Bandrauk, "Molecules in Intense Laser Fields," M. Dekker, New York (1994) Chapt. 1–3.
128 P. Dietrich, M. Yu. Ivanov, F. A. Ilkov, and P. B. Corkum, *Phys. Rev. Lett.*, **77**, 4150 (1996).
129 R. S. Mulliken, *J. Chem. Phys.*, **7**, 20 (1939).
130 Ionization rates of H_2^+ in static fields, as well as adiabatic energies, have been calculated by complex scaling methods. See, e.g., Z. Mulyukov, M. Pont, and R. Shakeshaft, *Phys. Rev. A*, **54**, 4299 (1996); M. Plummer, and J. F. McCann, *J. Phys. B*, **29**, 4625 (1996).
131 A. D. Bandrauk, *Comments At. Mol. Phys. D*, **1**, 97 (1999).
132 T. Zuo, and A. D. Bandrauk, *Phys. Rev. A*, **48**, 3837 (1993); *Phys. Rev. A*, **52**, R2511 (1995).
133 T. Seidemann, M. Y. Ivanov, and P. B. Corkum, *Phys. Rev. Lett.*, **75**, 2819 (1995).
134 I. Kawata, H. Kono, Y. Fujimura, and A. D. Bandrauk, *Phys. Rev. A*, **62**, 031401(R) (2000).
135 I. Kawata, A. D. Bandrauk, H. Kono, and Y. Fujimura, *Laser Physics*, **11**,188 (2001). An accurate calculation of adiabatic states of H_2 has been carried out. See, A. Saenz. *Phys. Rev. A*, **61**, 051402 (R) (2000).
136 E. B. Stechel and E. J. Heller, *Annu. Rev. Phys. Chem.*, **35**, 563 (1984).
137 H. Kono and N. Ohta, *J. Chem. Phys.*, **103**, 162 (1995).
138 H. Kono, Y. Fujimura, and A. D. Bandrauk, to be published.
139 G. N. Gibson, M. Li, C. Guo, and J. P. Nibarger, *Phys. Rev. A*, **58**, 4723 (1998).
140 A. D. Bandrauk, "The Physics of Electronic and Atomic Collisions," ed by Y. Itikawa et al., AIP Conf. Proc. 500, New York (1999), p. 102.
141 H. Kono, S. Koseki, M. Shiota, and Y. Fujimura, *J. Phys. Chem.*, in press.
142 K. Burnett, V. C. Reed, J. Cooper, and P. L. Knight, *Phys. Rev. A*, **45**, 3347 (1992).
143 J. L. Krause, K. J. Schafer, and K. C. Kulander, *Phys. Rev. A*, **45**, 4998 (1992).
144 A. Rundquist, G. Durfee III, Z.Chang, C.Herne, S. Backus, M. M. Murnane, and H. C. Kapteyn, *Science*, **280**, 1412 (1998).
145 F. Remacle and R. D. Levine, *J. Chem. Phys.*, **110**, 5089 (1999); F. Remacle and R. D. Levine, *J. Phys. Chem. A*, **104**, 2341 (2000).
146 J. M. Hopkins and W. Sibbett, *Scientific American*, September (2000).

Yukiyoshi Ohtsuki was born in Fukushima, Japan. He was graduated from Tohoku University in 1984 with B.S. degree in chemistry. He received his M.Sc. (1986) in physical chemistry from Kyoto University, and D.Sc. (1990) in physical chemistry from Tohoku University. His research interest is in the area of molecular quantum engineering, especially the development of methodology for solving quantum optimal control problems and the control of molecular dynamics in condensed phases. He is currently an assistant professor of Tohoku University.

Michihiko Sugawara was born in 1966 in Iwate. He received the B.Sc. and the M.Sc. degrees in chemistry from Tohoku University in 1998 and 1990, respectively. He also received the Ph.D. degree from Tohoku University in 1993. From 1993 to 1994, he was a JSPS Fellow. He was a Post-Doctoral Fellow at Arizona State University in 1994 and the Institute of Atomic and Molecular Science in 1995. Since 1995, he has been a Research Associate at Keio University. His research is concerned with theoretical study of molecular reaction control and computational chemistry.

Hirohiko Kono was born in Osaka in 1953. He received his Ph.D. in chemistry from Tohoku University in 1981. Since then, he joined the research group guided by Professor S. H. Lin at Arizona State University as postdoctoral fellow. In 1985, he became a Research Associate at Faculty of Engineering, Yamagata University. He was appointed as an associated Professor of College of General Education of Tohoku University in 1991. Since 1993 he has been Associate Professor of Department of Chemistry, Tohoku University. His current research includes electronic dynamics simulation of molecules in laser fields.

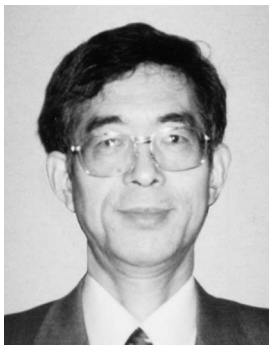

Yuichi Fujimura was born in Hokkaido in 1943. He received his B.Sc. degree from Yamagata University in 1966, and M.Sc. degree in chemistry from Kanazawa University in 1968. He also received his Ph.D. degree from Tohoku University in 1971. He became Research Associate of Department of Chemistry, Tohoku University in 1972, and Associate Professor of the same University in 1986. He was an Adjunction Associate Professor at Institute for Molecular Science from 1987 to 1988. Since 1995, he has been Professor of Department of Chemistry, Graduate School of Science, Tohoku University. His current research fields are theoretical studies of femtosecond chemistry and intense field chemistry.